Chapter: I

Introduction and Literature Review

Chapter – I

1.1 Introduction

Half doped manganese-based rare earth perovskite oxides, $R_{0.5}A_{0.5}MnO_3$ (A = La, Pr, Nd, Sm, Eu etc., A = Ca, Sr, Ba etc.), are investigated extensively in order to understand their structural behavior, magnetic properties, charge and orbital ordering which are often coupled, leading to complex physical properties [Dagotto (2003); Tokura (2000); Murakami (2003); Tokura et al. (2000); Dagotto et al. (2001)]. The beauty of the perovskite structure is that it can accommodate variety of the ions at A and B-sites with different valence and ionic sizes leading to widely different physical properties. The complex perovskite oxide material are special in their ability to possess variety of widely different physical properties such as ferromagnetic, ferroelectric, piezoelectric elecctro-optic, electrocatalytic, insulating semiconducting metallic etc. They also exhibit interesting phase transitions involving very rich physics and chemistry. Because of the wide range of physical properties, the multifunctional perovskite oxide, offer countless applications such as piezoelectric transducers and actuators, magnetic and ferroelectric memories, materials for electro-optic devices and optical fibers, positive temperature coefficient of resistence [Uchino (2000); Eerenstien et al. (2006)], colossal magnetoresistance [Coey et al. (1999)], hybrid solar and fuel cell [Minh et al. (1993)], phosphors and display devices, sensors etc.

This chapter presents a brief introduction of mixed valence perovskite manganites in general, with an emphasis on how the physical properties evolve as a function of composition and temperature, and the influence of crystal structure on controlling magnetic and transport properties in these materials. The physical properties of half doped perovskite manganites have been described and amongst the various phenomena exhibited by these compounds, magnetic phase transitions has been discussed in detail. Apart from these, possible modifications in physical properties which may arise as an outcome of crystallite size reduction in nanostructure compounds have been discussed.

1.2 Complex Structure and Properties of Perovskite Manganites

The mixed-valence perovskite manganese oxides, which are most commonly known as manganites, continue to be a central topic of research in condensed mater physics due to both scientific quest as well as promising technological applications [Rao et al. (1998); Dagotto (2002); Tokura (2006)]. Though manganite has extended history of research which started around middle of last century with the pioneering works by Jonker and Van Santen [Jonker et al. (1950)], Van Santen and Jonker [Van Santen et al. (1950)] Wollan and Koehler [Wollan et al. (1955)] etc., but it received renewed interest roughly two decades back after observation of colossal magnetoresistance (CMR), a phenomenon where zero field resistance could be suppressed by couple of orders upon application of magnetic field, opening possibilities for important technological applications. Moreover, this phenomenon has significance similar to high T_C superconductivity, which has been observed in cuprates another member of transition metal oxide (TMO) family. Furthermore, perovskite manganites exhibit rich phase diagrams, exhibiting a variety of phases, with unusual coupling between spin, charge, lattice and orbital orders, that has further motivated both experimentalists and theoreticians to improve their understanding related to structural, magnetic and transport properties in the electron correlated systems.

Physical properties in perovskite manganites with general formula $R_{1-x}A_xMnO_3$ where R and A are the rare earth trivalent (R = La^{3+}, Pr^{3+}, Nd^{3+}, Sm^{3+} etc.) and alkaline earth divalent (A = Ca^{2+}, Sr^{2+}, Ba^{2+} etc.) elements respectively, are mainly influenced by two important parameters: (i) band filling (or doping level), and (ii) e_g electron bandwidth. These both parameters can be controlled to a considerable extent by modifying the chemical composition, where the former is controlled by doping divalent atoms at R/A site and later is decided by the different combination of R-A ions which changes the structure as well as the Mn-O bond lengths and bond angles directly affecting the electron conduction in Mn-O-Mn network. The parent rare earth compounds with $x = 0$ are having only Mn^{3+} ions and show mostly antiferromagnetic (AFM) and insulating behavior (I) but with progressive hole doping equal amount of Mn^{4+} ions are created in the system and various electronic and magnetic phases evolve. The ferromagnetism observed in these systems beyond certain concentration of Mn^{4+} was explained by double exchange (DE) phenomenon, initially due to Zener [Zener (1951)], and later it was further extended by Anderson and Hasegawa [Anderson et al. (1955)] and De Gennes [De Gennes (1951)]. Though the DE mechanism, which linked the ferromagnetism (FM) and metallicity (M) was quite successful to explain various properties like ferromagnetism, CMR phenomenon metal-insulator transition in early days, but later on discrepancies were observed between the experimental results and theoretical predictions for several solid solutions. These include incorrect prediction for temperature variation of resistivity, wrong estimation of Curie temperature etc. and variety of interesting phenomenon like charge ordering (CO), orbital ordering (OO), ferromagnetic insulator, Jahn-Teller distortion etc. were invoked to explain the observed physical properties in manganites. Another addition to this list is the occurrence of phase sepration (PS), where the submicrometer size FM-M and AF-I phases coexist spontaneously [Dagotto (2002); Moreo et al. (1999)]. Phase separation in perovskite manganites has been studied extensively in both theoretical and experimental frontiers in last few years, and experimental evidence for the same has been provided for the manganites with various compositions [Dagotto (2002)]. Half doped (x = 0.5) compounds are found to be very susceptible to this phase coexistence phenomenon as they offer a comparable enegy scale for coexisting FM and AFM phases. Moreover, quenched disorder is found to have significant influence on phase separation, as recent simulation work has proposed chemical disorder driven inhomogeneous phase with coexistence of competing phases separated by first order transition metal oxides like cuprates and manganites [Burgi et al. (2001)], and quenched disorder induced certain modification of clusters [Burgi et al. (2000)]. The present thesis is motivated to study the effects of quenched disorder on phase separation in half doped mangaite, as well as to study related modification in physical properties.

1.3 General Description of Perovskite Oxide

The name perovskite oxide with general formula ABO_3 owes its origin to the mineral name ‘perovskite’ of the calcium titanate ($CaTiO_3$). The ideal perovskite structure belongs to the cubic crystal system in the $Pm3m$ space group (No. 221). The ions in the *Pm*3*m* space group occupy the Wyckoff positions as A in 1(a) sites at (0, 0, 0), B in 1(b) sites at (1/2,1/2,1/2) and O in 3(c) sites at (0, 1/2,1/2). In the ideal cubic perovskite structure, A and B ions are located at the centre of cubo-octahedron and octahedron respectively formed by the O ions. The sketche of the cubic perovskite structure is shown in Fig. 1.1. In 1962, Goldschmidt [Goldschmidt et al. (1926)] introduced a parameter 't' the now well known tolerance factor, to accurately describe the stability (deformability) of a perovskite structure. The expression for the factor 't', which associated with the ionic radius, is obtained by the concept of well-known closed packed theory of ions. It is given by

$$t = \frac{(R_A+R_O)}{\sqrt{2}(R_B+R_O)} \qquad 1.1$$

where, R_A, R_B and R_O correspond to the ionic radius of A, B and O atoms, respectively. For a stable perovskite structure, the value of 't' lies in the range $0.80<t<1.05$. For $t=1$, the structure is expected to adopt the ideal cubic symmetry. For $t>1$, the B atom is too small for the oxygen octahedron so that the structure will develop a small polar distortion, as in $BaTiO_3$. Conversely, when $t<1$, the A atom is small for the oxygen cubo-octahedral coordination and cannot effectively bond with all twelve neighboring O atoms. If 't' is only slightly less than one, rotations and tilting of the oxygen octahedra will be favored (as in $SrTiO_3$ and $CaTiO_3$).

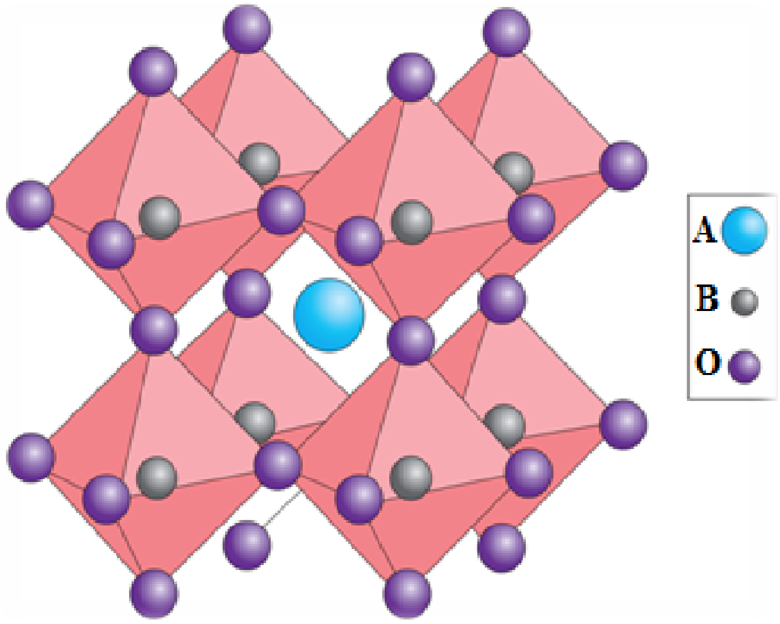

Fig. 1.1. Ideal ABO_3 perovskite unit cell depicting 'A' ions at (0, 0, 0), the 'B' ions (1/2, 1/2, 1/2) and 'O' ions at (0, 1/2, 1/2) positions in cubic lattice.

1.4 Classification of Magnetic Materials

The variety of magnetic properties exhibited in different classes of materials offers much scope for experimental as well as theoretical hypothesis. The magnetic properties of solids originate due to motion of the electrons and due to permanent magnetic moments of the atoms and electrons.Magnetic behavior is determined primarily by the electronic structure of a material, which provides magnetic dipoles (circulating charges behave like magnetic dipoles). Sometimes we are also interested in nuclear magnetism which can be explained on the basis of nucleons present in the system. Magnetic moments the nuclei are of the order of 10^{-3} times smaller than the magnetic moment of electrons and are thus insignificant in most of the cases. The magnetic moment of a free atom has three principle sources: the spin with which the electrons are endowed; their orbital angular momentum about the nucleus; and the change in the orbital moment induced by an externally applied magnetic field. The magnetic moment is a vector quantity, parallel to the axis of the spin and normal to the plane of the orbit, respectively. The magnetic moment of an atom is the vector sum of all its magnetic moments and following possibilities arise leading to various classes of magnetism.

1.4.1 Diamagnetism

Diamagnetism is a small and very weak effect in many materials mainly due to the influence of the applied magnetic field on the orbiting electrons in accordance with Lenz’s law so that the magnetization and the susceptibility are both negative. Electrons which constitute a closed shell in an atom usually have their spin and orbital moments so oriented that the atom as a whole has no net moment. Bi, Hg, Au, Cu are some examples of diamagnetic substances. If a magnetic material is subjected to magnetic field, it can increase or decrease the flux density. Diamagnetic materials reduce the density of lines of forces and this effect is produced by the circulation of electrons in atoms. Normally for diamagnetic substances $\chi<0$ and it is independent of temperature. Superconductors in which electrons make cooper pairs are perfect diamagnets with $\chi = -1$.

1.4.2 Paramagnetism

Diamagnetism is an intrinsic characteristic of all matter but presence of other types of magnetism is a result of the fact that many atoms have a permanent magnetic dipole moment which overbalances the diamagnetic effect. In some materials, the permanent magnetic moments of the atoms have no mutual interaction among them, this effect is called paramagnetism. However, in the presence of external magnetic field, the magnetic moments have tendency to turn towards the direction of the field. If no opposing force acts, complete alignment of the magnetic moments will be there and the specimen would acquire very large magnetization in the direction of the field, however thermal agitation tries to keep the magnetic dipole moments at random and it results only a partial alignment in the field direction. Effectively materials with atoms of unpaired electron spins are paramagnetic.

1.4.3 Ferromagnetism

Ferromagnetism is defined as the presence of spontaneous magnetization in the absence of an external magnetic field whose orientation can be switched hysterically by the externally applied magnetic field. The origin of the spontaneous magnetization is due to an internal ‘molecular field’ which tends to align the magnetic moments parallel to each other [Cullity (1972)]. The origin of the molecular field has been found to be quantum mechanical exchange energy, which causes electrons with parallel spins (and therefore parallel magnetic moments) to have a lower energy than electrons with parallel spins in the ferromagnetic materials. As ferromagnetic materials are heated, the degree of alignment of the atomic magnetic moments decreases i.e. it becomes disordered and the ferromagnetic materials transform to paramagnetic at higher temperatures. The temperature at which this transition takes place is known as the Curie temperature (T_C). The saturation magnetization goes to zero at the Curie temperature. Above T_C the susceptibility varies according to the Curie-Weiss law given by

$$\chi = \frac{C}{T - T_C} \tag{1.2}$$

As-prepared samples of ferromagnetic materials often lack a macroscopic magnetization because of the presence of domains of magnetization oriented in different direction to minimize the energy of the system. The subsequent alignment and reorientation of the domains, upon the application of a magnetic field (H), results in a hysteresis in the magnetization (M) and applied magnetic field H as shown in Fig. 1.2.

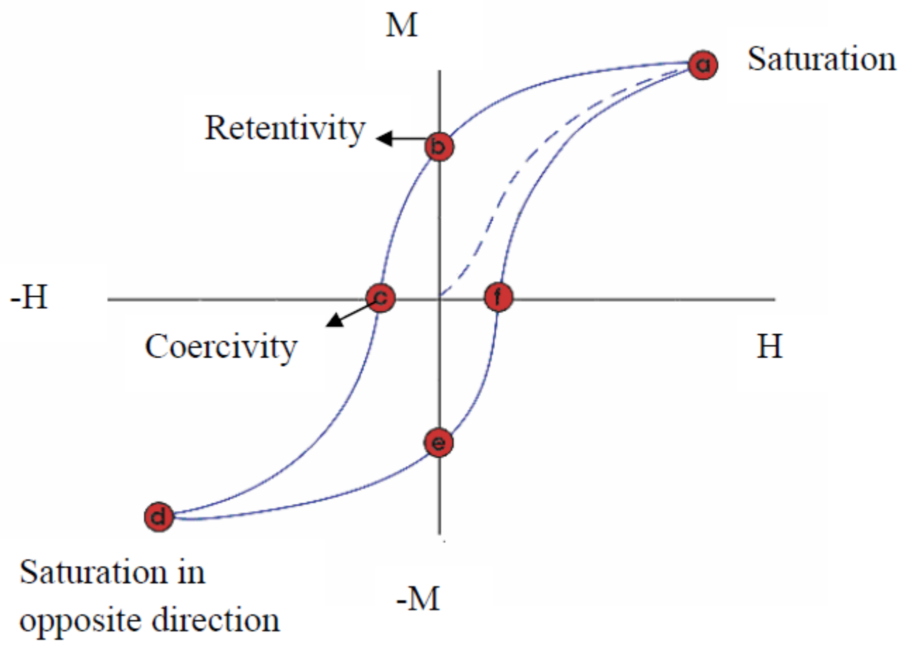

Fig.1.2. Typical M-H hysteresis loop for ferromagnetic materials [after Cullity (1972)]

1.4.4 Antiferromagnetism

When the alignment of the spin moments of neighbouring atoms is antiparallel to each other, it is termed as antiferromagnetism. The exchange interaction in this case favours antiparallel alignment of the spins. No net magnetic moment is associated in this case, since there is a total cancellation of both spin and orbital moments.

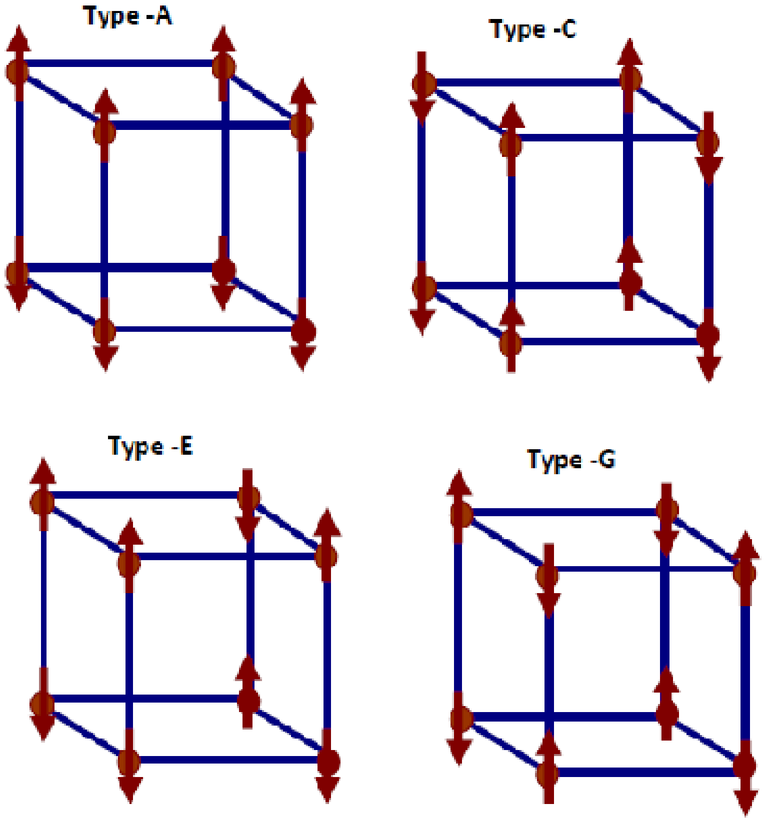

Fig. 1.3. Different types of lattice arrangement resulting in different type (A-, C-, G- and E-type) antiferromagnetic ordering [drawn using convention of Wollen et al. (1955)].

There are several ways of arranging an equal number of up and down spins depending on the kind of crystal lattice on which the spins are to be arranged. These types of arrangements result in different types of antiferromagnetic ordering (A-, C-, G-, or E-type) as shown in Fig. 1.3. Antiferromagnetic order vanishes above a critical temperature known as the Neel temperature. Above the Neel temperature (T_N), the material behaves like a typical paramagnet. Below T_N, due to lower thermal energy as compared to the gain due to antiparallel ordering of neighbouring spins, the antiferromagnetic state is formed. A plot of inverse of susceptibility (χ^{-1}) versus temperature (T) is a straight line in antiferromagnets also, just like ferromagnets, above T_N but this line extrapolates to negative Curie temperature ($-T_C$) at $1/\chi=0$. Above T_N, it obeys the Curie-Weiss law.

Although, one does not expect net magnetization in the antiferromagnetic materials, it may exhibit net magnetization due to spin canting, lattice defects, and, frustrated surface spins in the absence of magnetic field. At sufficiently high magnetic fields, the spin direction of one of the magnetic sublattices may rotate and eventually lead to the ‘spin flop’ where all the spins would be aligned in a parallel fashion. Because of this rotation and spin flop, magnetization can be induced by an external magnetic field. The temperature dependence of the magnetization (M) and χ^{-1} for different types of magnetic materials (ferromagnetic and antiferromagnetic) are shown in Fig. 1.4 (a) and (b).

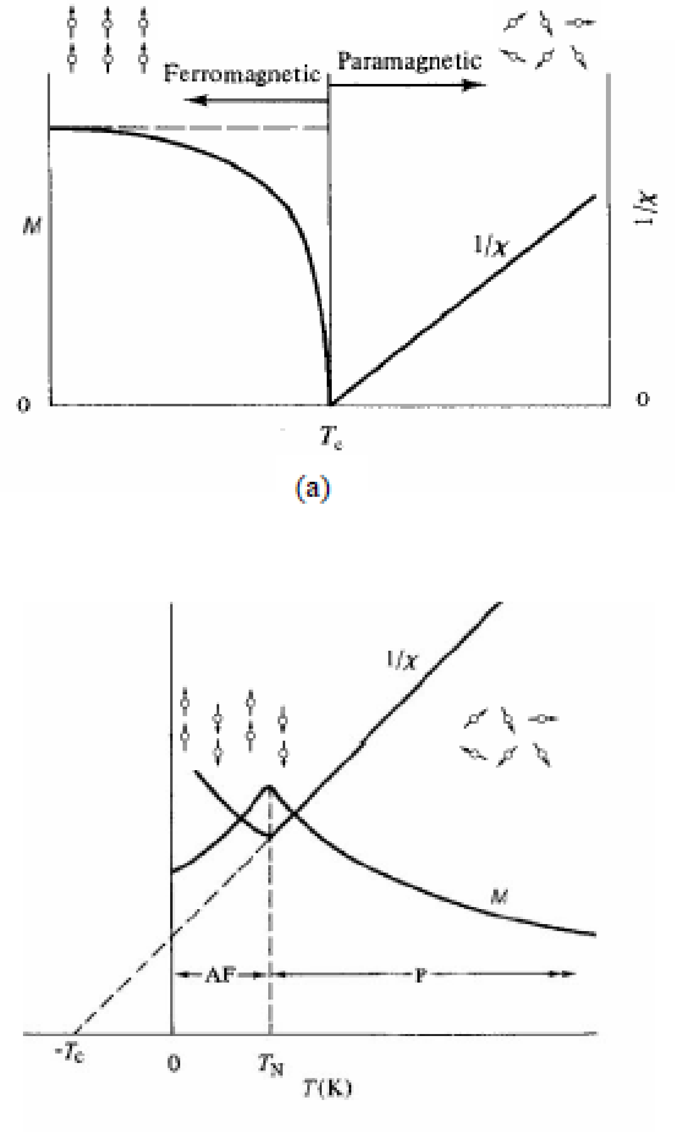

(a)

(b)

Fig.1.4. Temperature dependence of magnetization (M) and the inverse of the magnetic susceptibility (χ^{-1}) for (a) ferromagnetic and (b) antiferromagnetic material (schematic). AF = antiferromagnetic and P = paramagnetic [after Cullity (1972)].

1.5 Magnetic Interactions

Quantum mechanical exchange interactions are responsible for the phenomenon of long range magnetic order. The coupling of magnetic moments, which is quantum mechanical in nature, is known as exchange interaction and is essentially an out come of overlap of electronic orbitals keeping in mind the Pauli's exclusion principle. Exchange interactions are in some sense like electrostatic interactions, arising because charges of same sign cost energy when they are close together and save energy when they are apart. We list below the different types of exchange interactions which lead to long range magnetic order state.

1.5.1 Direct Exchange

When the electrons on neighbouring magnetic ions, which are close enough to have sufficient overlap of their wave functions, interact via exchange interaction, it is known as direct exchange. It gives a strong short range coupling, which reduces rapidly on increasing the separation between the magnetic ions. For direct exchange interaction, the exchange integral J_{ex} can be positive or negative depending upon the balance between Coulombic and kinetic energies. In the frame work of Ising model [Cullity (1972)]

$$E_{ex} = -J_{ex} S_i . S_j \qquad 1.3$$

where E_{ex} is the exchange energy, S_i and S_j are the electronic spins at the atomic sites which can take values +1/2 or -1/2. Thus for, two atoms with one electron each, when the atoms are very close to each other, the Coulomb interaction is minimal when the electrons spend most of their time in between the nuclei. Since the electrons are then required to be at the same place in space at the same time, then according to Pauli's exclusion principle, it is necessary for them to possess anti-parallel spins. This gives rise to anti-parallel alignment i.e. antiferromagnetic ordering and therefore negative exchange interaction Jex in Eq. (1.3). But, if the atoms are far apart, the electrons spend their time away from each other in order to minimize the electron-electron Coulombic repulsion. This can give rise to parallel alignment, i.e. ferromagnetism, with positive exchange interaction. The nature of direct exchange interaction can be determined using the Bethe-Slater curve shown in Fig.1.5 which represents the magnitude and sign of exchange integral (J_{ex}) as a function of inter-atomic distance.

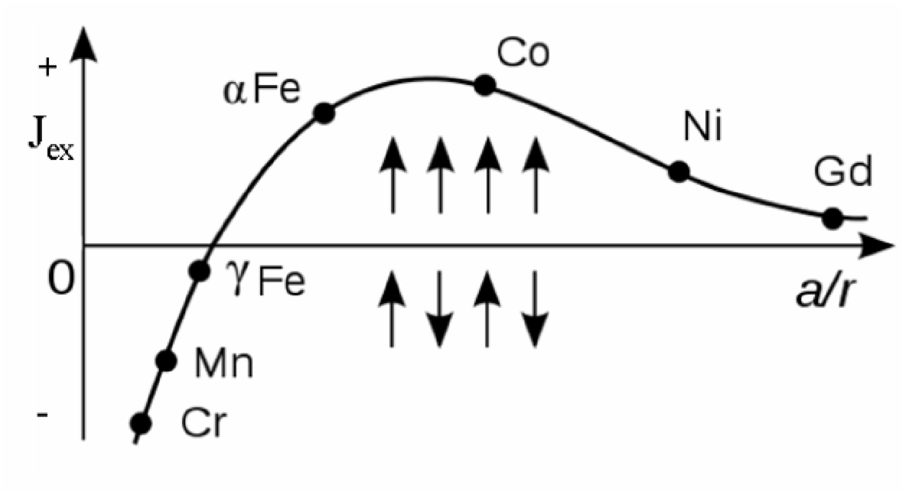

Fig.1.5. Bathe-Slater curve (schematic) ‘a’ is the radius of an atom and r is the radius of its 3d shell of electrons [after Cullity (1972)].

1.5.2 Indirect Exchange

The interaction between magnetic ions can also be mediated by the conduction electrons. A localized magnetic moment spin-polarizes the conduction electrons and this polarization in turn couples to a neighbouring localized magnetic moment at a distance ‘r’. The exchange interaction is thus an indirect one because it does not involve direct coupling between the magnetic moments. This type of interaction is commonly known as Ruderman-Kittel-Kasua-Yoshida RKKY interaction (or also as itinerant exchange interaction) [Ruderman et al. (1954); Kasuya (1956); Yosida et al. (1957)], named after the discoveres of the effect. The RKKY type exchange coupling JRKKY (r) is given by [Blundel (2001)]

$$J_{RKKY}(r) \propto \mathrm{Cos}\,(2k_F r)/r^3 \qquad 1.4$$

at large r (assuming a spherical Fermi surface of radius k_F). The RKKY interaction shown in Fig.1.6 is long ranged and has a damped oscillatory (oscillates between positive and negative values) dependence on the separation between the magnetic moments. Therefore, depending upon the separation between a pair of magnetic ions, coupling between them can be of ferromagnetic or antiferromagnetic nature.

1.5.3 Super exchange interaction

Superexchange describes the interaction between moments of ions which are too far apart to be influence by direct exchange, but couple over a relatively long distance through a non-magnetic ion which is placed in between the magnetic ions [Anderson (1950)]. For example, MnO and MnF_2 are both antiferromagnets, though there is no direct overlap between the electrons on Mn^{2+} ions in each system.

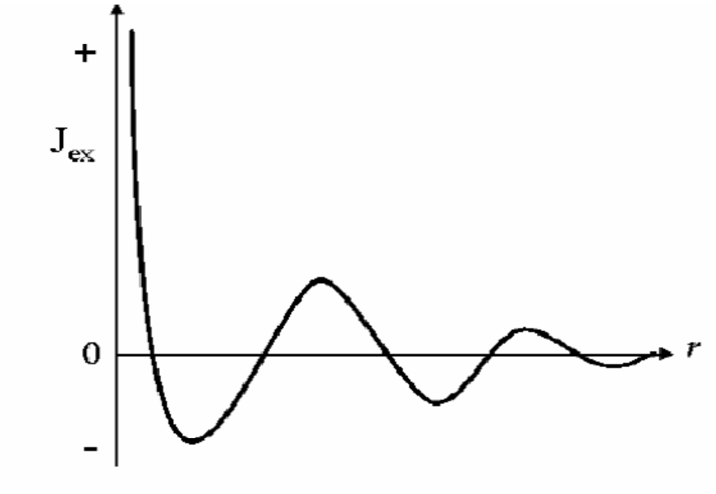

Fig.1.6 The coefficient of RKKY versus the inter-atomic distance r [after Rutheman et al. (1954)].

If the system is perfectly ionic, each metal ion would have a single unpaired electron in a d-orbital whereas oxygen have two p electrons in its outer most occupied states. The strength of the anti-parallel coupling between metal ions (M) depends on the bond angle M-O-M and is generally greatest when this angle is 180^o i.e. the spins are collinear.

1.5.4 Double Exchange Interaction

In some oxides, it is possible to have a ferromagnetic exchange interaction due to the occurrence of magnetic ions showing mixed valency i.e., it can exist in more than one oxidation state. For example, Mn ion which can exist in oxidation states +3 or +4, i.e., as Mn^{3+} or Mn^{4+}, in the mixed manganite system $La_{1-x}Sr_xMnO_3$. The ferromagnetic alignment in such systems is due to the double exchange mechanism [Zener (1951)] and can be understood with reference to Fig.1.7. In the case of mixed valency of Mn ion, e_g electron on Mn^{3+} ion can hop to a neighbouring site Mn^{4+} via oxygen by interacting with 2p electrons of O^{2-}. This is possible only if there is a vacancy of the same spin. However, because of the strong Hund's coupling, the three electrons in the t_{2g} level want to keep the e_g electron aligned to them. Thus it is not energetically favourable for an e_g electron to hop to a neighbouring ion in which the t_{2g} spins will be antiparallel to the e_g electron. Ferromagnetic alignment of neighbouring ions is required to maintain the high-spin arrangement on both the donating and the receiving ions. This model is superficially similar to superexchange.

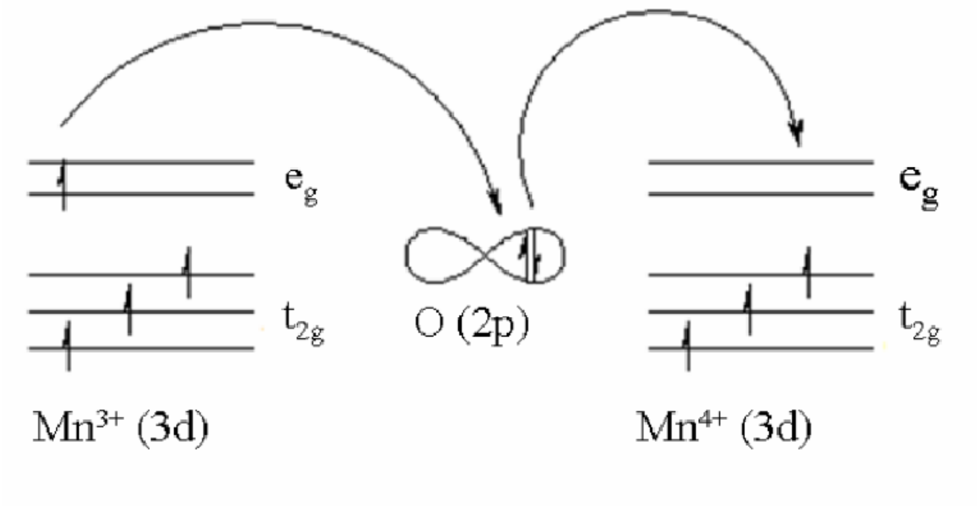

Fig. 1.7. Schematic representation of double exchange interaction [after Zener et al. (1951)]

In superexchange, an antiferromagnetic (in general) or ferromagnetic alignment occurs between two atoms with the same valence, while in double exchange, the interaction occurs only when one atom has an extra electron compared to the other.

1.6 Crystal Field Splitting and Jahn-Teller Distortion

Physical properties in perovskite manganites in the form of $AMnO_3$ (A being rare earth elements) are largely decided by MnO_6 octahedra, which forms a basic building block in this structure. In Fig. 1.1 schematic perovskite structure is depicted. Usually in isolated manganese atom, five orbitals in d-level are degenerate but when the Mn ion is surrounded by six oxygen's in regular octahedral environment of crystal, degeneracy is lifted and five levels are split in two groups with energy difference Δ_{oct} (= 1 to 2 eV), the lower triplet t_{2g} and upper doublet e_g. This occurs due to electrostatic interaction between d-electrons of Mn ion and surrounding negative legand ions (Oxygen). The doubly degenerate e_g orbitlas ($d_{x^2-y^2}$ and d_{z^2}) point along the directions where the negative oxygen ions are located, thus increasing the energy due to Coulombic repulsion. On the other hand, triply degenerate t_{2g} orbitals (d_{xy}, d_{yz} and d_{zx}) point in the directions between the legands where fields are less, and therefore stabilized in lower energy. This situation is schematically depicted in Fig. 1.8, as the successive electrons are introduced in d-shell of Mn-ion. They occupy the lowest Mn ion available orbitals compatible with total spin associated as in present case, ions of Mn^{3+} and Mn^{4+}, so their electronic configurations are $t_{2g}^3 e_g^1$ and $t_{2g}^3 e_g^0$ respectively.

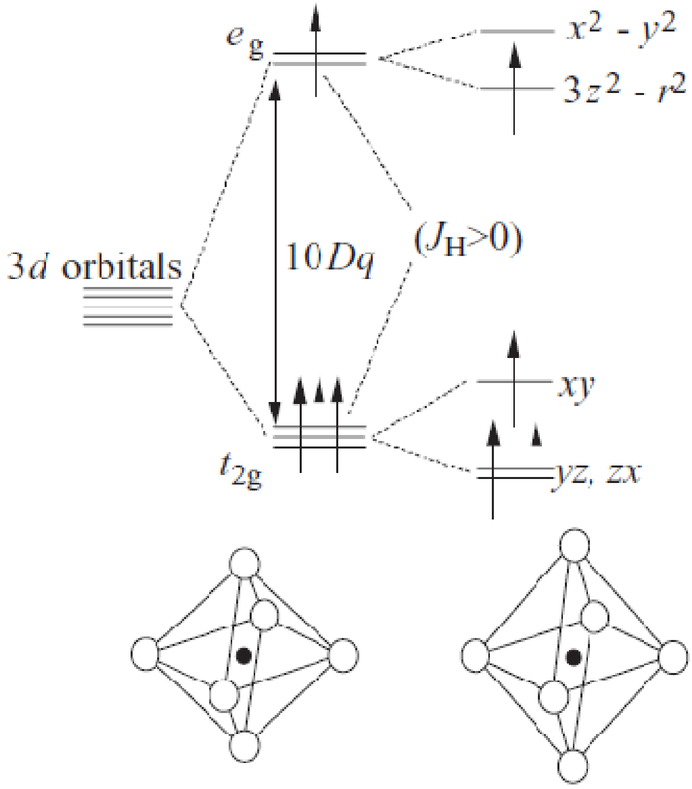

Fig. 1.8. Crystal-field splitting of the five-fold degenerate atomic 3d levels into lower t_{2g} (triply degenerate) and higher e_g (doubly degenerate) levels. The Jahn–Teller distortion of the MnO_6 octahedron further lifts each degeneracy [after Tokura (2006)].

As discussed above the crystal field effect lead to split in d orbitals into an e_g doublet and t_{2g} triplet, the remaining degeneracy is further lifted by Jahn Teller distortion [Jahn et al. (1937)]. Jahn Teller distortion showed that, if the electronic state of a non-linear molecules is orbitally degenerate, then there is always at least one vibrational coordinate along which the molecule may distort, so as to lower its energy. The situation can be exemplified for Mn^{3+}. The presence of single electron in doubly degenerate e_g orbitals can distort the octahedron where the surrounding oxygen atoms can slightly readjust their locations, creating an asymmetry between the different directions that effectively removes the degeneracy. This is known as Jahn Teller distortion which is found to have crucial role in stabilizing various phases in perovskite manganites. MnO_6 octahedra is distorted in such a way that the center of gravity of the t_{2g} levels and that of e_g levels is unchanged. This is manifested in the form of basel planes distortion with one diagonally opposite oxygen pair is displaced outwards and other pair is displaced inside or basel plane oxygens are displaced inside and apical oxygens are displaced outside. This distortion can be static as observed in manganites in smaller hole density, or dynamic namely a given ion is not frozen in one distorted configurations evolve among several configurations as a function of time. However, this distortion splits e_g band opening a gap in Fermi level.

1.7 Complex Ordering Phenomena in Perovskite Manganites

With the strong correlation effect, electrons that normally localize on specific atomic sites, frequently exhibit cooperative electronic ordering phenomena, i.e. charge order, orbital order and spin order in the perovskite manganites [Tokura et al. (2006), Rao et al. (2000)]. These novel quantum collective behaviors are usually accompanied by concomitant structural, magnetic and metal-insulator phase transitions and so forth. Thus they are believed to play significant roles in controlling these fascinating physical properties.

1.7.1 Charge Ordering

The physics of manganite perovskites has been studied intensively in recent years following the discovery of CMR in many compositions. The charge ordered (CO) ground state is most easily observed in half-doped manganites. The model for this CO phase was proposed by Goodenough (1955) after the magnetic structure had been found to be the complex CE-type antiferromagnetic couplings along zigzag chains. The CO in doped perovskite manganite is characterized by an ordering of Mn^{3+} and Mn^{4+} species within the MnO_2 plane, causing the localization of e_g electrons and the antiferromagnetic(AFM) spin ordering below the CO transition temperature T_{CO} [Tokura (2006)]. The CO phenomenon represents one of the most interesting issues in these materials due to the strong interactions among the charge, spin, orbital and lattice degrees of freedom and has been studied intensively. The charge-ordered phases are novel manifestations arising from the interaction between the charge carriers and the phonons. Charge ordering arises because the carriers are localized into specific sites below a certain temperature, T_{CO}, giving rise to long-range order through-out the crystal structure.

1.7.2 Orbital Ordering

Orbital order in perovskite manganites can occur at certain carrier concentrations when the d-electrons occupy an asymmetric orbital. The driving force is partly direct electrostatic repulsion of the charge clouds, but coupled Jahn-Teller distortions of adjacent octahedral stabilize the effect. Goodenough (1955) proposed that this ordering would entail displacements of the $Mn^{+4}O_6$ octahedra. In particular, we will show in subsequent chapters that the development of magnetic ordering is associated with the appearance of weak reflections in the x-ray diffraction patterns, which are the signature of small structural distortions due to charge and orbital ordering. It was found that, in agreement with Goodenough’s hypothesis, the super structure is characterized by a large J-T distortion of the $Mn^{3+}O_6$ octahedra, while the $Mn^{4+}O_6$ octahedra remain almost undistorted [Goodenough (1955)]. Furthermore, orbital ordering occurs by a displacement of the $Mn^{4+}O_6$ octahedra mainly along the [0 0 1] direction. The $Mn^{3+\cdot}e_g$ orbitals ($3dz^2$) and the associated lattice distortions (long Mn–O bonds) also develop long-range order, giving rise to orbital ordering. Thus, at low temperatures, the rare earth perovskite manganites are antiferromagnetically ordered (AFM) with CE or A type ordering, but only the former occurs in the charge-ordered materials where the e_g electrons are localized. The CE-type spin ordering is characterized by the ordering of $Mn^{3+}$and Mn^{4+} ions alternately.

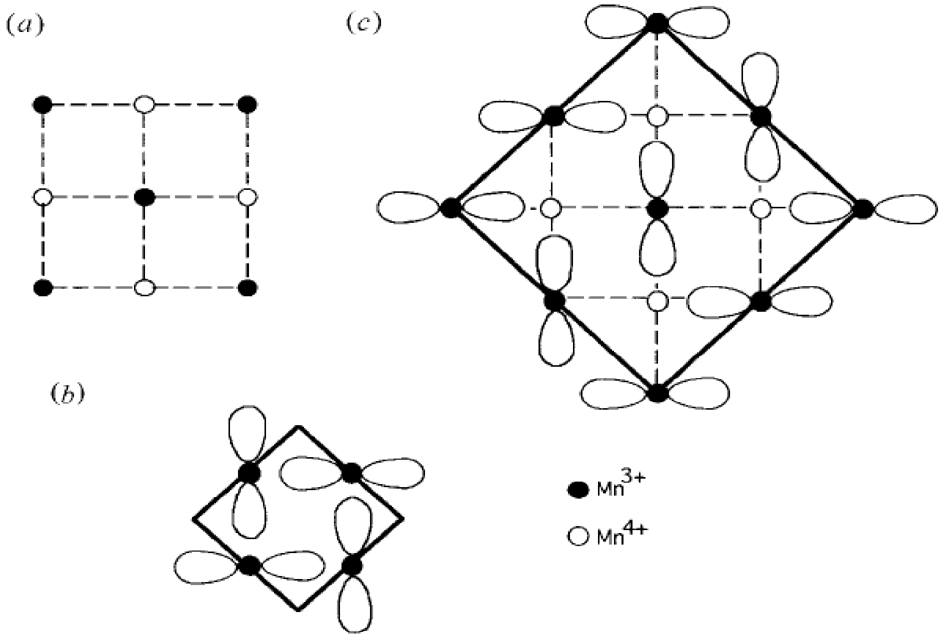

Fig. 1.9. (a) - Charge ordering of Mn^{3+} and Mn^{4+} in a mixed crystal with x=1/2 (b) Orbital ordering of the d_z^2 orbitals of Mn^{3+} when x=0, (c) Combined charge and orbital ordering when x=1/2 [after Rao et al. (2000)].

1.8 Magnetoresistance

Magnetoresistive effects are nowadays a very interesting topic in both applied and fundamental physics. Their importance was first related to technological applications mainly in magnetic recording or magnetic data storage. However, soon it was noticed that it is sufficiently valuable to study these phenomena in detail from a purely scientific point of view. Magnetoresistance is the relative change in the electrical resistance of a material on the application of magnetic field. Mathematical expression can be given as-

$$\mathrm{MR}\,(H, 0) = [\rho(H{=}0T)-\rho(H)] / \rho(H{=}\,0T) \qquad -1.4$$

Depending on the relative change in resistivity on applying magnetic field, it is called either as Giant magnetoresistance (GMR) or Colossal magnetoresistance (CMR) [Tokura (2006)].

1.8.1 Colossal Magnetoresistance (CMR)

In the early 1990s a new kind of MR was rediscovered in mixed-valence perovskite manganites. The electrical transport constitutes probably the most attractive physical property of these manganites. The physics of CMR in manganites is decided by strength of spin interactions which is strongly dependent on the doping level and temperature. At room temperature, $Nd_{1-x}Sr_xMnO_3$ shows the FM state for $0.3 < x < 0.5$. When doped further, the compound shows the A-type AFM state for $0.5 < x < 0.7$ related to the bad metal features which are widely observed in the conducting transition-metal oxides with strong electron–electron (electron correlation) and/or electron–lattice interactions. The correlated electrons, which are almost localized on the respective atomic sites, bear three attributes, namely, charge, spin and orbital degrees of freedom. The conduction electrons with an orbital degree of freedom are scattered not only by the strong electron correlation (or spin correlation dependent) effect but also by the strong electron–lattice coupling due to Jahn–Teller interaction. The collective or local Jahn–Teller distortions, as described by the displacement of the oxygen ions surrounding Mn sites, are observed everywhere when the compound shows the dramatic resistive (e.g. insulator-to-metal) or magnetic (e.g. antiferromagnetic-to ferromagnetic) transitions [Tokura (2006)]. The possibility of phase in homogeneity or phase separation has often been argued as the essential ingredient in CMR physics.

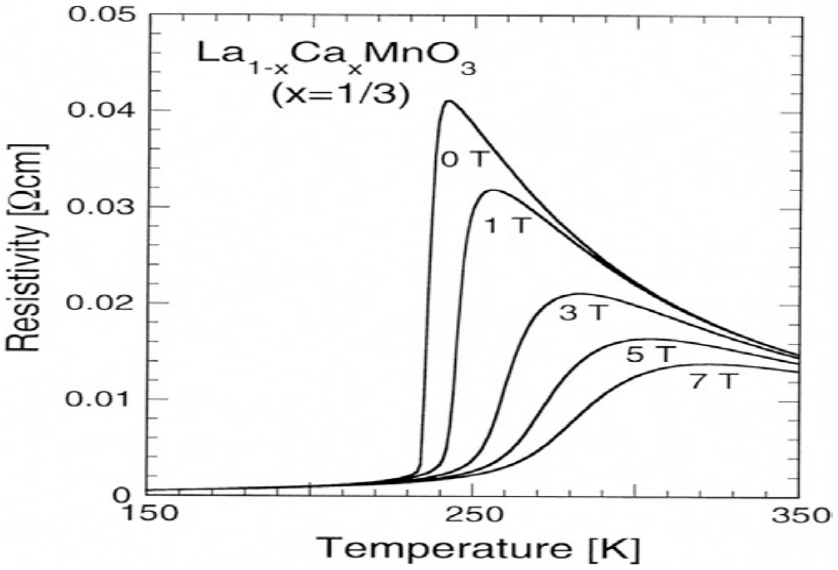

Fig.1.10. Colossal magnetoresistance (CMR) behavior for the $La_{0.67}Ca_{0.33}MnO_3$ [after Tokura (2006)]

1.8.2 Giant Magnetoresistance (GMR)

Almost parallel to the study of the intrinsic CMR, a new kind of MR was discovered in granular manganites samples called GMR. This effect is completely absent in single crystals, and was rapidly related to spin-polarized tunnelling between neighboring grains. For this reason it is usually denoted as intergranular MR (IMR) [Baibich et al. (1988)]. There are great similarities between this MR and the already studied one in ferromagnetic/insulator and ferromagnetic/metal alloys, but the MR values reported in these last cases are much higher. The main explanation of this GMR lies again in the intrinsic properties of manganites, derived from their special electronic configuration [Binasch et al. (1989)]. Generally, in a ferromagnet, the band structure is spin dependent, and two sub bands are found for majority (spin parallel to the magnetization) and minority (spin antiparallel to the magnetization) spins. As a result, a net spin polarization (P) takes place. In perovskite manganites, there exists a gap in the density of states of minority carriers, and so the total spin polarization is 1. In the spin tunneling model, GMR depends critically on the spin polarization, and hence the higher P values in manganites lead to higher MR values than those reported for other ferromagnetic alloys [Baibich et al. (1988)].

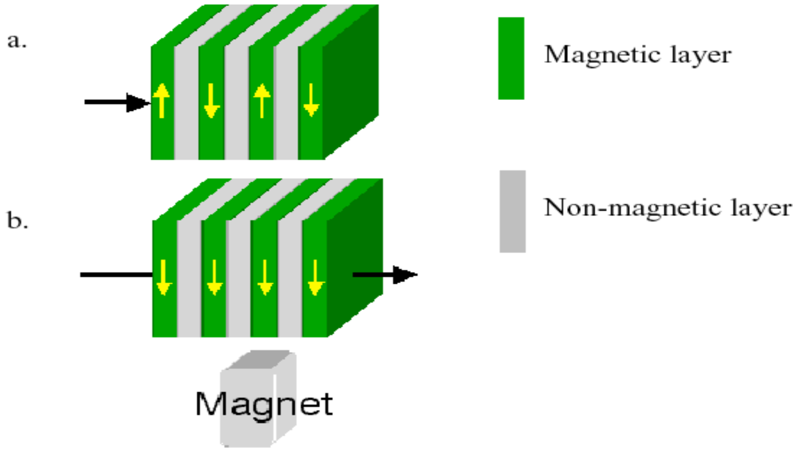

Fig. 1.11. GMR materials are made from alternating layers of magnetic and non magnetic metals that are nanometers in thickness. [drawn using convention of Binasch et al. (1989)].

1.9 Review of Crystal Structure and Magnetism in Mixed-Valence Perovskite Manganites

Complex interplay between spin, charge, phase separation and orbital degrees of freedom and their role on magnetic state and phase transition behavior of doped rare earth perovskite manganites have made them very fascinating for researchers from several decades [Coey et al. (1999); Wang et al. (1999); Levy et al. (2000); Loudon et al. (2002); Tomioka et al. (2000); Rao et al. (1998); Park et al. (2006); Dagotto et al. (2001); Xiong et al. (2004); Wollan et al. (1955); Lees et al. (1996); Kawano et al. (1996); Jirak et al. (1990) and Jirak et al. (1996)]. It is recently reported in several doped rare earth manganites that when the particle size is reduced to nanoscale, the low temperature charge and orbitally ordered insulating state is destabilized, with suppression of charge ordering transition and stabilization of high temperature ferromagnetic metallic state down to low temperatures [Liu et al. (2009); Rao et al. (2005); Kundu et al. (2012); Giri et al. (2014); Zhou et al. (2013); Markovich et al. (2011); Zhou et al. (2011); Zhou and Guo et al. (2011); Zhang et al. (2010); Wang et al. (2010); Chai et al. (2009)]. Apart from crystallite size, stabilization of ferromagnetic metallic phase and suppression of insulating charge ordering transition in manganites is also reported by a number of other external perturbations such as magnetic field [Kuwahara et al. (1995)], biaxial strain, pressure [Kozlenko et al. (2004)], and in some cases even electric field [Asamitsu et al. (1997); Guha et al. (1999)]. In case of $La_{0.5}Ca_{0.5}MnO_3$ [LCMO] it is reported that the charge ordered state is completely absent when the particle size is less than 40 nm [Sarkar et al. (2008)]. The suppression of charge ordering transition is reported in nanocrystalline form of several other half doped manganites also such as $Pr_{0.5}Ca_{0.5}MnO_3$ [PCMO] [Zhang et al. (2009)], $Nd_{0.5}C_{0.5}MnO_3$ [NCMO] [Rao et al. (2006)], $Nd_{0.5}Sr_{0.5}MnO_3$ [NSMO] [Biswas et al. (2007)], $Pr_{0.5}Sr_{0.5}MnO_3$ [PSMO] [Pramanik et al. (2010)] so and forth. In the subsequent sections we present a brief overview of the broad features of selected half doped mixed valence perovskite manganites with general formula $R_{1-x}A_xMnO_3$ (R = rare earth and A = alkaline), that are investigated in the present thesis for crystal structure and magnetic phase transition behaviour as a function of crystallite size.

1.9.1 Magnetic and Phase Transition Behaviour of $La_{1-x}Ca_xMnO_3$ Manganites

The $La_{1-x}Ca_xMnO_3$ [LCMO] is the most extensively investigated perovskite manganite. The complete phase diagram of $La_{1-x}Ca_xMnO_3$, obtained using magnetization and resistivity data is shown in Fig. 1.12 reproduced from Cheong and Hwang [Cheong and Hwang et al. (1999)]. This phase diagram is established by working with relatively a small set of samples with varying Ca concentrations. Fig.1.12 clearly illustrates that many phases are in competition in this system. Very prominent is the ferromagnetic metallic phase, at lower temperature which is widely believed to be caused by double exchange interaction mechanism where mobile electrons polarize the localized spins to increase their kinetic energy, as in the Nagaoka Phase of cuprates [Nagaoka (1966)]. However, equally prominent is the charge ordered (CO) regime at hole densities larger than 50%. The ferromagnetic (FM) vs antiferromagnetic/charge ordered/orbital ordered competition is believed to be at the heart of the curious magneto-transport properties of many manganites [Dagotto et al. (2001)]. The presence of antiferromagnetic phase clearly shows that the double exchange interaction and related ideas are not sufficient to explain the properties of low or intermediate band width manganites since in the double exchange (DE) context there is no room for such AF/CO/OO phases at low temperature.

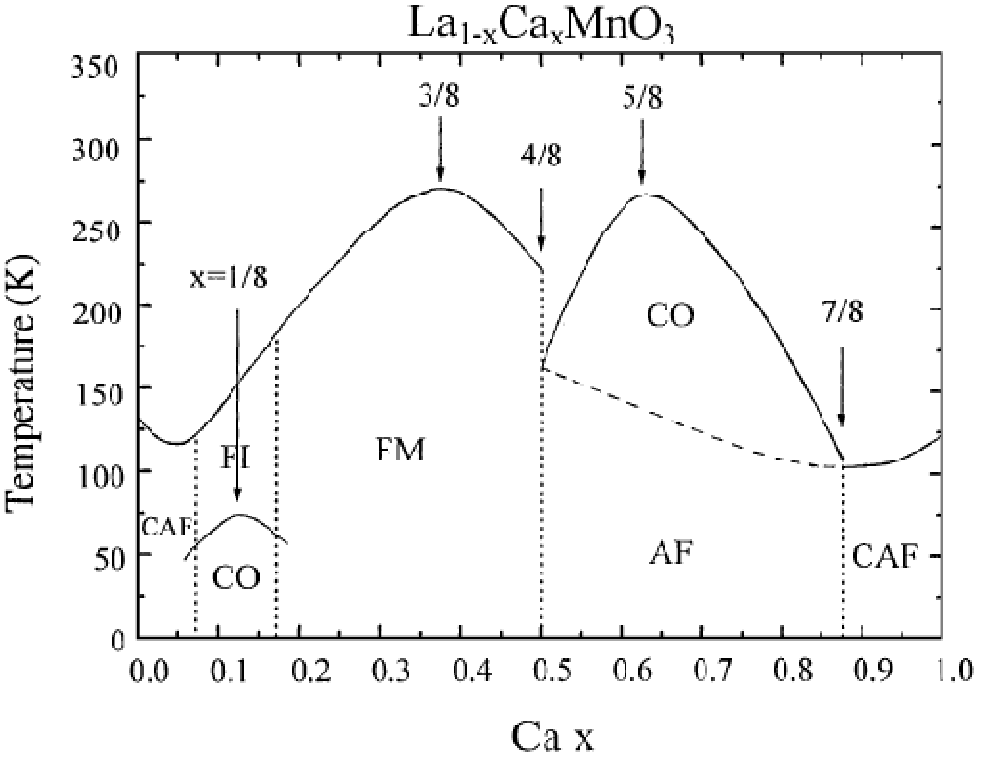

Fig. 1.12. Phase diagram of $La_{1-x}Ca_xMnO_3$, constructed from measurements of macroscopic quantities such as the resistivity and magnetic susceptibility, FM: Ferromagnetic Metal, FI: Ferromagnetic Insulator, AF: Antiferromagnetic, CAF: Canted AF, and CO: Charge/Orbital Ordered. FI and/or CAF could be spatially inhomogeneous states with FM and AF coexistence [after Cheong et al. (1999)].

At low hole density, a completed regime with FI (ferromagnetic insulator), CO (charge ordered) and CAF (canted antiferromagnetic phases) is reached. In LCMO system the regime of doping where the CMR effects can be found, there is low temperature FM metallic phase. The CMR occurs particularly at the boundaries of metallic phase. This shows clearly that it is the competition between metallic and insulator phases that causes CMR, and is likely not an intrinsic property of any of the phases in isolation. In fact, results in the regime of electron doping support this view. Large magnetoresistance (MR) has been observed at the composition about 85% when the FM and AF phases are in competition [Mahendiran et al. (1996); Chiba et al. (1996); Maignan et al. (1998); Martin et al. (1997)]. It is not necessary to work at the FM metallic phase of low hole density to find a large MR. The Ca concentrations (x) at multiples of 1/8, which were highlighted by Cheong and Hwang [Cheong et al. (1999)], are important for the physics of manganites. This is clearly of relevance at $x = 3/8$ and 5/8 where the FM and CO maximum critical temperatures are obtained. The phase diagram also shows that double exchange ideas, which at large Hund coupling leads to a phase diagram mirror symmetric between $x<0.5$ and $x>0.5$, are not suitable to describe these materials. In fact, the phase diagram has a clear electron hole asymmetry. For end compositions with $x = 0.0$ and $x = 1.0$, the ground state is antiferromagnetic. At $x = 0.0$ it is A-type (FM in two directions and AF in other direction), while at $x = 1.0$ it is G-type (AF in three directions).

1.9.2 Lattice parameter, Unit Cell Volume, Magnetization and Resistivity variation in $La_{0.5}Ca_{0.5}MnO_3$ Manganites

In LCMO system the composition with x = 0.50 is very interesting and has been extensively investigated. This composition shows much larger changes in the lattice parameters at the magnetic transitions. Variation of magnetization, resistivity and lattice parameters with temperature is shown in Fig. 1.13. Throughout a relatively broad region with an onset at ~220 K the b- lattice parameter drastically decreases, while those along the ‘a’ and ‘c’ axes increase. This behavior is accompanied by an increase of the strain in a-c plane, i.e., $O_{\|} = 2(c-a)/(c+a)$. The onsets of the increase of ‘a’ and ‘c’ and of the decrease of the ‘b’ parameter are associated with the inflection point in the M(T) curve, defining the ferromagnetic transition. It is remarkable that no transition is observed in the unit cell volume (V) *vs* Temperature (T) curve. The subsequent intermediate regime of magnetization spans an interval of ~50 K, which is just in the range where a rapid decrease of the ‘b’ axis and increase of the ‘a’ and ‘c’ axes occur. The sharp drop in the M(T) curve occurring at ~170 K, accompany a sharp increase of resistivity,

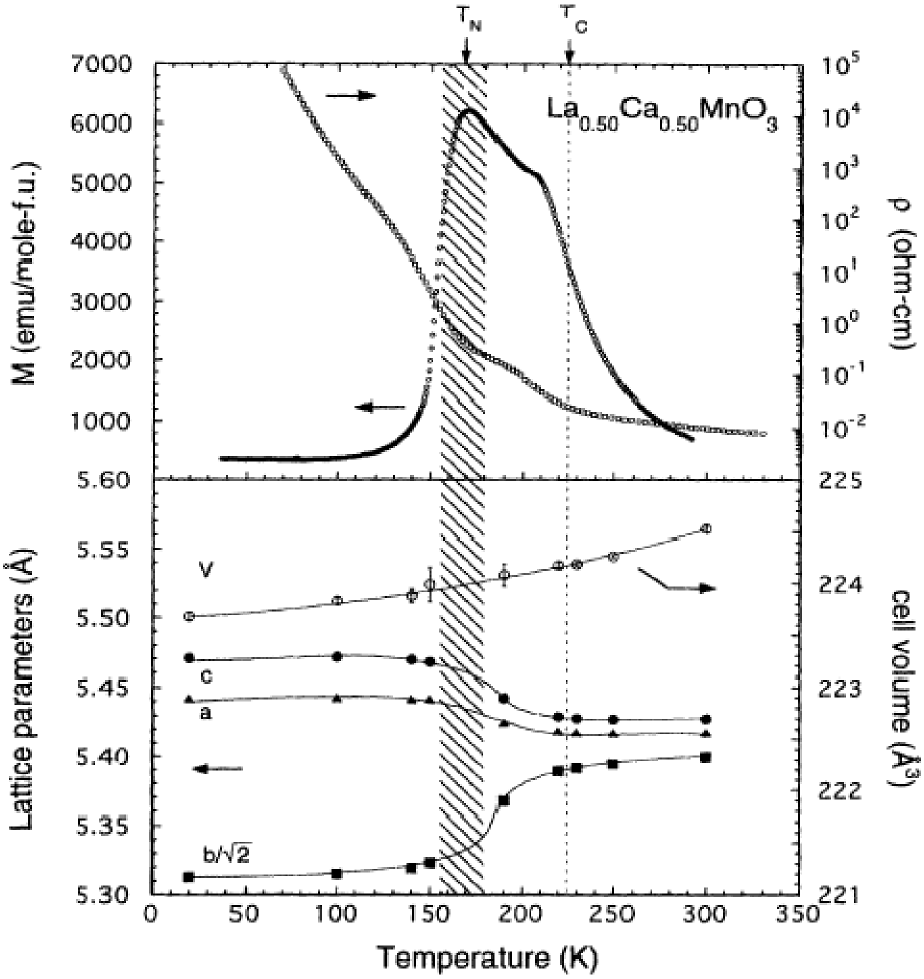

Fig. 1.13. (Lower panel) Lattice parameters and cell volume as a function of temperature for the $La_{0.5}Ca_{0.5}MnO_3$ sample, measured on cooling. Lines through the points are guides to the eye. The shaded area represents the width of the magnetization hysteresis loop. (Upper panel) Magnetization (H = 1 T) and electric resistivity (H = 0 T) vs T for $La_{0.5}Ca_{0.5}MnO_3$ measured on cooling [after Radaelli et al. (1995)].

1.9.3 Structure and Magnetization of Nanocrystalline $La_{0.5}Ca_{0.5}MnO_3$ Manganites

Sarkar et al. (2008) recently reported significant changes in the structure and magnetic properties of nanocrystalline $La_{0.5}Ca_{0.5}MnO_3$. Temperature evolution of the lattice parameters for the bulk as well as for the nanoparticle reported by Sarkar et al. (2008) is shown in Fig. 1.14. The structure is orthorhombic (space group *Pnma)* for both the bulk and nanocrystalline samples. In contrast to the bulk samples, for the nano sample, the lattice parameters virtually remain unchanged throughout the temperature range studied. The small changes in the lattice parameters of the nanoparticles on cooling do not follow any systematic trend, unlike that in the bulk sample. As per the reports of Sarkar et al. (2008) in the nanoparticles, the 'a' axis at room temperature is smaller by $\approx 1\%$, the b axis is smaller by $\approx 2\%$, while the c axis expands by $\approx 1\%$.

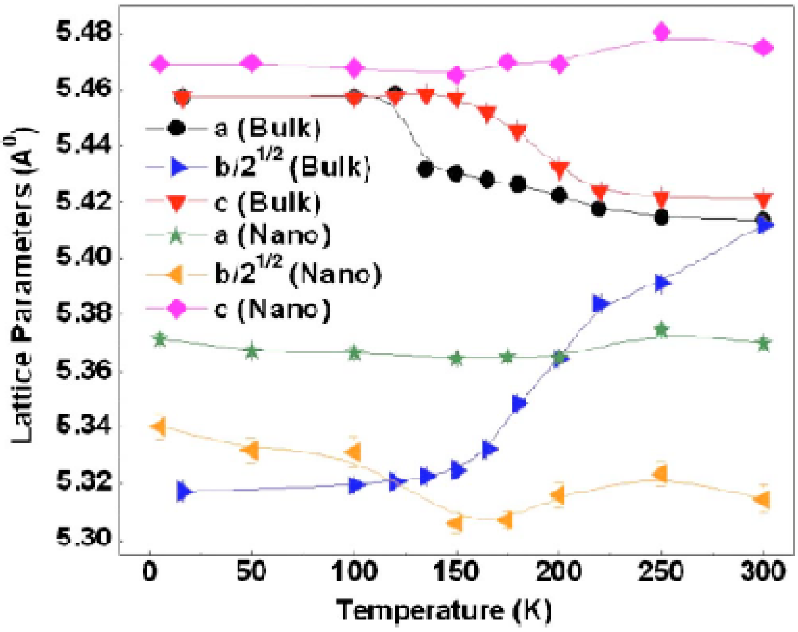

Fig. 1.14. Variation of lattice parameters of bulk and nanocrystalline half doped $La_{0.5}Ca_{0.5}MnO_3$ manganites with measuring temperature [after Sarkar et al. (2008)].

Variation of the cell volume and the orthorhombic strains $OS_{\parallel}$ and $OS_{\perp}$ in the two samples reported by Sarkar et al. (2008) are shown in Fig. 1.15.The cell volume is reported to decrease by about 1.6% in the nanoparticle sample. The orthorhombic strain $OS_{\parallel}$ gives the strain in the ac plane and is defined as $OS_{\parallel} = 2(c-a)/(c+a)$, while $OS_{\perp}$ gives the strain along the b- axis with respect to the ac- plane and is defined as $OS_{\perp} = 2(a+c-\sqrt{b})/(a+c+\sqrt{b})$. In the bulk sample, the largest change occurs in $OS_{\perp}$, which increases as the sample is cooled and reaches a saturating value of 0.026 below the charge ordering temperature T_{CO}. On the other hand, $OS_{\parallel}$ shows a modest value over the whole temperature range. It shows a small enhancement in the temperature range $T_{CO}<T<T_C$ and decreases to nearly 0 for $T<T_{CO}$. On the other hand, in the nanoparticle sample, the orthorhombic strains are isotropic ($OS_{\perp} \approx OS_{\parallel}$), and they remain more or less temperature independent [Sarkar et al. (2008)]. No clear changes can be detected near any of the transitions.

Sarkar et al. (2008) reported that reduction of the particle size suppresses charge ordering transition and the room temperature structure is stabilized at lower temperatures also. The size induced arrest of the structure in nano-LCMO is reflected in its physical properties, which shows that the CO transition is destabilized and the ferromagnetic state becomes stable at low temperatures. Fig. 1.16 shows the field cooled magnetization versus temperature data for bulk and nano samples reported by Sarkar et al. (2008) under two magnetic fields, 0.01 T [inset (a) of Fig. 1.16], and 5 T. Inset (b) of Fig. 1.16 shows the ac susceptibility data. The bulk sample, as expected, shows the ferromagnetic transition and a sudden drop in the magnetization at ~155 K,

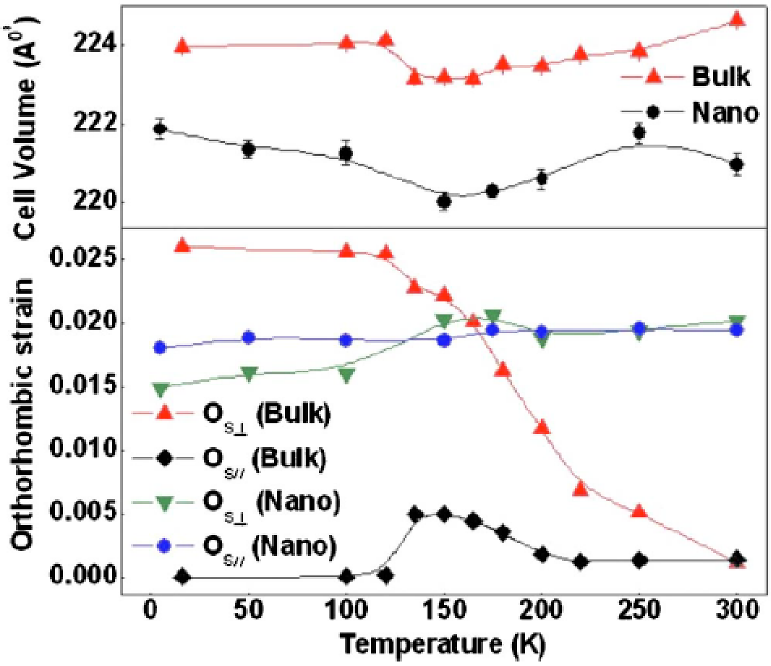

Fig. 1.15. Variation of Unit Cell Volume and Orthorhombic starin of bulk and nanocrystalline half doped $La_{0.5}Ca_{0.5}MnO_3$ manganites with measuring temperature [after Sarkar et al. (2008)].

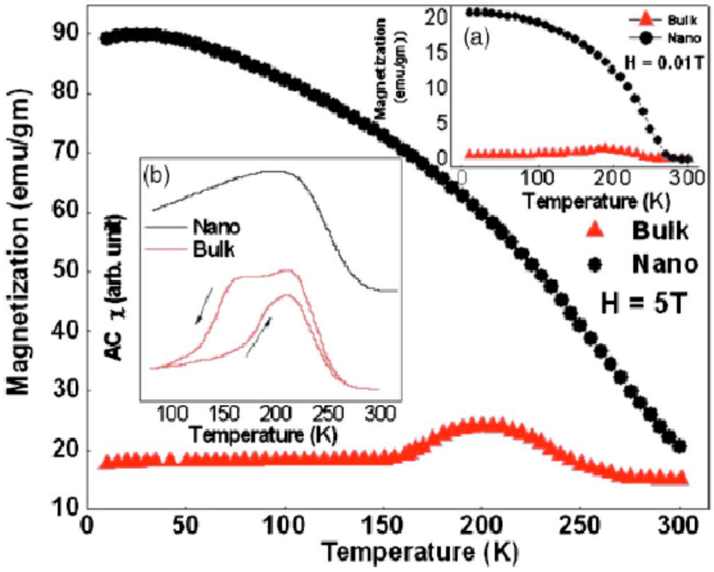

Fig. 1.16. Temperature variation of magnetization for bulk and nanocrystalline half doped $La_{0.5}Ca_{0.5}MnO_3$ manganites [after Sarkar et al. (2008)].

indicating the presence of the antiferromagnetic transition which accompanies the charge ordering transition. The hysteresis in the ac susceptibility seen in the bulk sample near T_{CO} is a signature of the transition. On the other hand in the nanoparticle sample, no such signature of any antiferromagnetic transition is seen. In contrast, in the nanocrystals, the ferromagnetic behavior that sets in at $T_C \approx 255$ K remains stable until the lowest measured temperature of 10 K with a total ferromagnetic moment of 3.18 μ_B/ f.u., which is 91% of the expected moment considering full ferromagnetic alignment of spins [Sarkar et al. (2008)]. This sample also shows a clear hysteresis loop in the M- H curve with a coercive field of 400 Oe at T = 5 K, which is the same as seen in ferromagnetic compositions, of $La_{0.5}Ca_{0.5}MnO_3$.

Recently, in another report by Iniama et al. (2014) it was shown that cell volume first decreases with annealing temperature of nano samples shows a minimum at sample annealing temperature, T_a = 900 ºC; then, increases up to reaching a maximum for bulk samples. Fig. 1.17 shows the variation of crystallite size and unit cell volume with sample annealing temperature (T_a) reported by Iniama et al. (2014). Surprisingly, cell volume in these nanoparticles is always smaller than cell volume of bulk, a behavior which is unusual in most of the $Ln_{1-x}A_xMnO_3$ compounds [Rao et al. (2006); Rao et al. (2005); Zhang et al. (2007)]. Sarkar et al (2008) also reported a smaller cell volume for $La_{0.5}Ca_{0.5}MnO_3$ with 15nm particle size, which increases continuously with annealing temperature, up to reaching a bulk value for particle size at micrometer range. Iniama et al. (2014) reported that XRD peak widths decrease as T_a increases, indicating an increase of the average crystallite sizes. The crystallite size is found to be around ~15 nm for LC700, then slightly increases to 16 nm for LC800 and finally reaches 22 nm for LC900 [see Fig. 1.17(b)]. By heating the sample at 1000 ºC, the crystallite size increases markedly to 40 nm, suggesting the beginning of a sintering process. Fig. 1.18 shows the variation of unit cell volume and saturation magnetization Ms^{FM} for $La_{0.5}Ca_{0.5}MnO_3$ nanocrystals and bulk reported by Iniama et al. (2014). It is evident that Ms^{FM} enhancement is related to cell volume decrease and both can be explained by an increase of hydrostatic pressure in the nanocrystals. Therefore, an effective pressure could cause crystal structure to deviate from bulk structure and favors FM ordering at expense of AFM one.

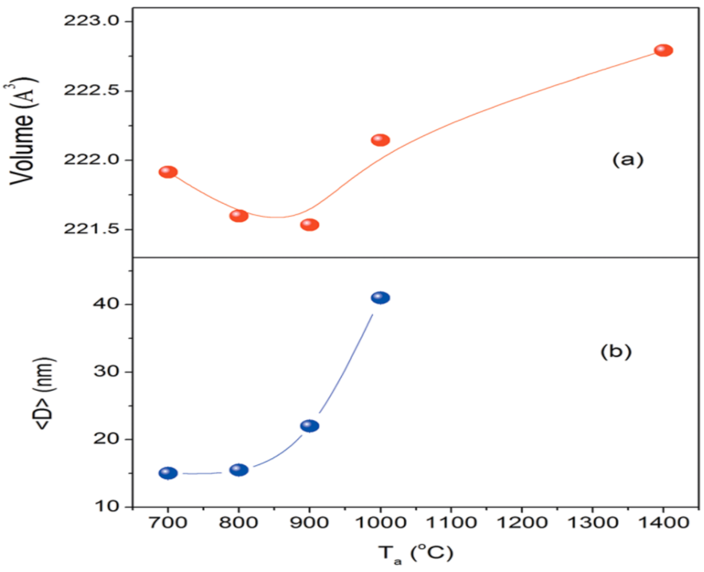

Fig. 1.17 (a) Variation of unit cell volume as a function of annealing temperature for $La_{0.5}Ca_{0.5}MnO_3$ (b) Mean crystallite size calculated by Scherrer's formula [after Iniama et al. (2014)].

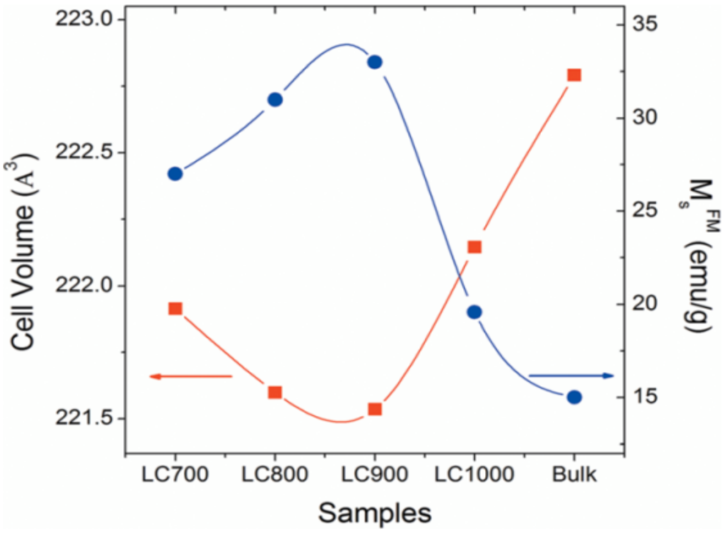

Fig. 1.18. Variation of unit cell volume (squares) and saturation magnetization (Ms) (circles) for $La_{0.5}Ca_{0.5}MnO_3$ samples LC700, LC900, LC1000, and Bulk [after Iniama et al. (2014)].

Iniama et al. (2014) proposed that FM ordering comes mainly from atoms at crystallite boundaries but there exists another FM contribution originated from hydrostatic pressure inside the crystallites that enhances FM ordering. The ZFC-FC magnetization measurements on LCMO samples at H = 1000 Oe reported by Iniama et al. (2014) is shown in Fig. 1.19. All the samples undergo a transition from paramagnetic to ferromagnetic state at around 230–250 K, where T_C shown in the inset to Fig. 1.19 is identified by a minimum in the dM/dT curves. At low temperature, ZFC and FC curves differ and finally converge at a different temperature for each sample, well below T_C, a typical behavior for spin glass transitions is seen. Spin-glass like transition, where a change from a state of disordered spins undergoes to a magnetic state with ordered magnetic spins, fits in a multidomain nanoparticles scenario in which

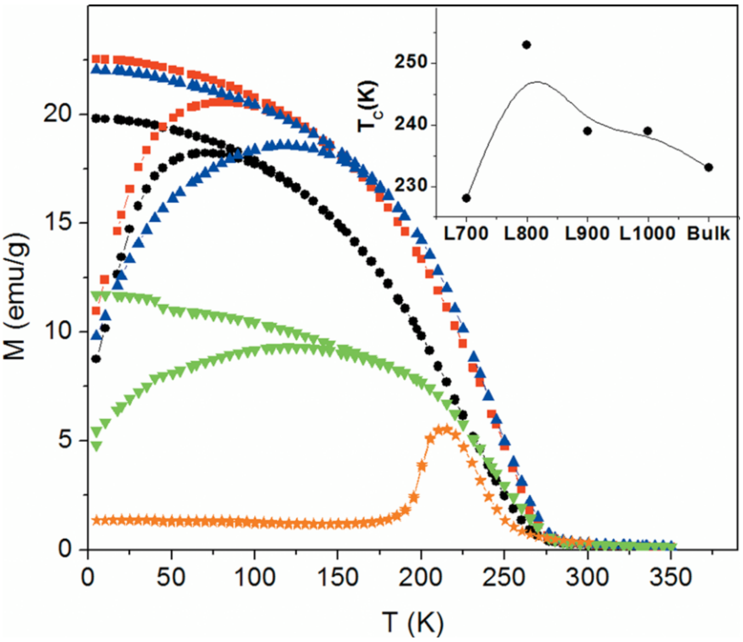

Fig 1.19. ZFC-FC curves measured at H = 1000 Oe for LC700 (circles), LC800 (squares), LC900 (up triangles), LC1000 (down triangles), and bulk (stars) samples. The inset shows the Curie temperatures for each sample [after Iniama et al. (2014)].

.

crystallite boundaries with FM like behavior surrounds very crystalline AFM cores due to presence of a kind of “core-shell” structure [Zhang et al. (2007); Crespo et al. (2013)]. Several studies suggest that the surface effects, like different composition at grain boundaries or low degree of crystallinity, bear on different ways to the interaction between magnetic moments of neighboring grains or between magnetic moments inside grains and surface spins in nanocrystalline samples [Mi et al. (2007); Lopez et al. (2014)]. As discussed in the foregoing the unit cell volume for nanocrystalline LCMO samples reported by Sarkar et al. (2008) and Iniama et al. (2014) are not in agreement. In another report Jirak et al. (2010) have shown that nano smaples of LCMO have larger unit cell volume than the bulk samples. We will show in chapter III that unit cell volume of nanocrystalline LCMO is very sensitive to stoichiometry of the samples and can decide the magnetic state of the samples.

1.9.4 Magnetic and Phase Transition Behaviour of $Nd_{1-x}Sr_xMnO_3$ Manganites

The system $Nd_{1-x}Sr_xMnO_3$ has a rich phase diagram, where paramagnetism (*P*) ferromagnetism (FM), antiferromagnetism (AFM), and orbital and charge ordering (CO) are determined by the temperature and the doping level (*x*). We begin with the description of the overall features of the lattice and magnetic structure of the $Nd_{1-x}Sr_xMnO_3$ system by examining the x–T phase diagram for $0.3 \leq x \leq 0.8$ reported by Kuwahara et al. (2003) and Kajimoto et al. (1999) shown in Figs. 1.20 and 1.21. In the distorted perovskite crystal structure, Mn ions are surrounded by six O ions, and the MnO_6 octahedra form pseudo-cubic lattice, whereas Nd or Sr ions occupy the bodycenter position of the pseudo-cubic lattice of the MnO_6 octahedra due to the buckling of the octahedra. However, the orthorhombic unit cell becomes $\sqrt{2} \times \sqrt{2} \times 2$ of the cubic cell. In the concentration region for $0.3 \leq x \leq 0.8$, the crystal structure is classified into two phases from the lattice parameters. The one is a well-known O′ phase with $c/\sqrt{2} < b < a$, [Zirak et al. (1985)] and appears in the lower Sr -concentration region for $x \leq 0.55$ at room temperature, while the other is a pseudo-tetragonal O‡ phase with $a \simeq b < c/\sqrt{2}$ for $x \geq 0.55$ as indicated in the Fig. 1.20. At low temperatures, on the other hand, the region of the O′ phase expands, and the phase boundary shifts towards around $x = 0.60$. In addition, a monoclinic structure is detected near the low temperature structural phase boundary around $x \sim 0.60$. For $0.55 \leq x \leq 0.60$, a structural transition from the O′ phase to the O‡ phase coincides with the AFM transition temperature T_N.

For $x < 0.48$, the ground state is a FM metal. In the region for $0.50 \leq x \leq 0.60$, there appears a metallic AFM state with the layered type AFM ordering, which is called as A-type after Wollan et al. (1955). With further increasing x, the C-type AFM order was observed in the O‡ phase. In this phase, the resistivity uniformly increases with lowering temperature, and the sample remains insulating for all temperatures, although the temperature derivative of the resistivity shows an anomaly at T_N [Kuwahara et al (1998)]. Only within a small range of the Sr concentration around $x \sim 0.50$, the system exhibits a charge-ordered insulating state which is accompanied with the CE-type AFM spin ordering after it shows the metallic FM state below T_C in the intermediate temperature region.

The structural and magnetic aspects of bulk $Nd_{0.5}Sr_{0.5}MnO_3$ (NSMO) has been investigated extensively by earlier authors [Ritter et al. (2000); Tomioka et al. (1995); Kuwahara et al. (1998); Eremenko et al. (2001); Kajimoto et al. (1999)]. Ritter et al [Ritter et al. (2000)] suggested that the lower temperature antiferromagnetic insulating charge ordered phase is phase segregated into two different crystallographic structures and three magnetic phases, orthorhombic (*Imma*) ferromagnetic, orthorhombic (*Imma*) antiferromagnetic and monoclinic ($P2_1/m$) charge ordered CE type antiferromagnetic. Externally applied magnetic field of sufficient strength can transform the charge ordered monoclinic phase to collapse into ferromagnetic metallic phase in orthorhombic symmetry [Tomioka et al. (1995)]. Other groups showed that in $Nd_{0.5}Sr_{0.5}MnO_3$, during transition from ferromagnetic metallic to antiferromagnetic insulating charge ordered state, the crystal symmetry is lowered to monoclinic $P2_1/m$ [Kuwahara et al. (1998); Eremenko et al. (2001)]. Kajimoto et al [Kajimoto et al. (1999)] showed that in the CE type and A-type antiferromagnetic states, the MnO_6 octahedra are apically compressed corresponding to $d_{3x^2-r^2}/d_{3y^2-r^2}$ or $d_{x^2-y^2}$ orbital ordering.

1.9.5 Structures and Phase Transitions in $Nd_{1-x}Sr_xMnO_3$ Manganites

Fig. 1.21 reveals that crystallographic phase diagram for $Nd_{1-x}Sr_xMnO_3$ crystal ($0.50 \leq x \leq 0.80$) reported by Kuwahara et al (2003). The metallic state with layered (A-type) AF state appears for $0.51 \leq x \leq 0.62$. Doping above $x = 0.62$ further alters the magnetic structures to the chain type.

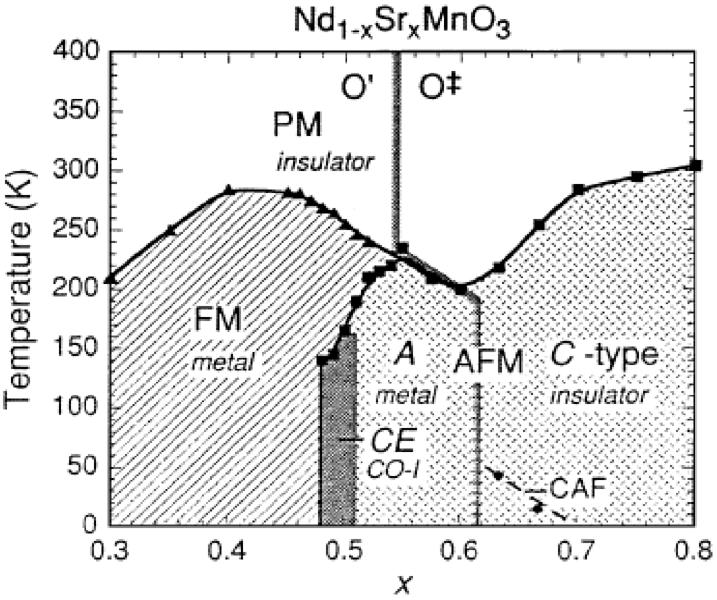

Fig. 1.20. Magnetic Phase diagram for $Nd_{1-x}Sr_xMnO_3$ crystal ($0.30 \leq x \leq 0.80$) [after Kajimoto et al. (1999)].

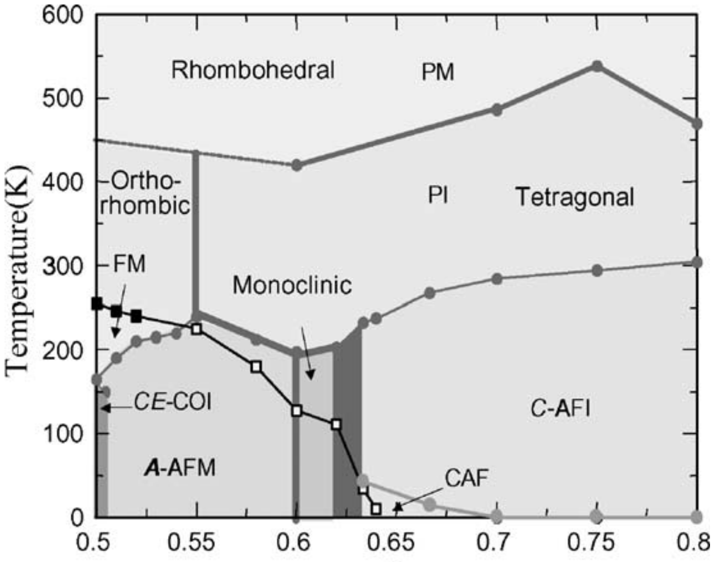

Fig. 1.21. Crystallographic Phase diagram for $Nd_{1-x}Sr_xMnO_3$ crystal ($0.50 \leq x \leq 0.80$). [after Kuwahara et al. (2003)].

The phase separation near this phase boundary (broad line near at x = 0.625) between the A-type-AF metal has monoclinic crystal symmetry and the C-type-AF insulator has tetragonal structure. As shown in the figure, spin ordering is decoupled from the orbital degree of freedom similar to the case of the parent material $LaMnO_3$. The thick lines located around ~450 K denote the phase boundary between the orbital-ordered insulator with tetragonal symmetry in low-temperature phase and orbital-disordered metal with rhombohedral one in high-temperature phase [Kuwahara et al. (2003)].

1.9.6 Lattice parameter, Unit Cell Volume, Magnetization and Resistivity variation in $Nd_{0.5}Sr_{0.5}MnO_3$ Manganites

Fig. 1.22 shows the temperature variation of magnetization, lattice parameter and resistivity for the charge/orbital ordering transitions observed for $Nd_{1-x}Sr_xMnO_3$ (x = 0.5) [Kuwahara et al. (1995), Tokura et al. (1999)]. As shown in Fig. 1.22, in the temperature dependence of resistivity and magnetization, the charge/orbital ordering transitions manifest themselves as decrease in magnetization and increase in resistivity, at $T_{CO}(=T_N) \approx 160$ K in $Nd_{0.5}Sr_{0.5}MnO_3$. Changes in lattice parameters are also observed at T_{CO}. Elongation in the orthorhombic a- and b-axes and contraction in the c-axis is seen, which suggests that ordering of e_g-orbital occurs simultaneously. Such a change in lattice parameters upon the charge/orbital ordering transition has also been reported for polycrystalline $La_{0.5}Ca_{0.5}MnO_3$ (T_{CO} $(=T_N) \approx 160$ K) [Radaelli et al (1995); Radaelli et al. (1997)], as shown in Fig. 1.13.

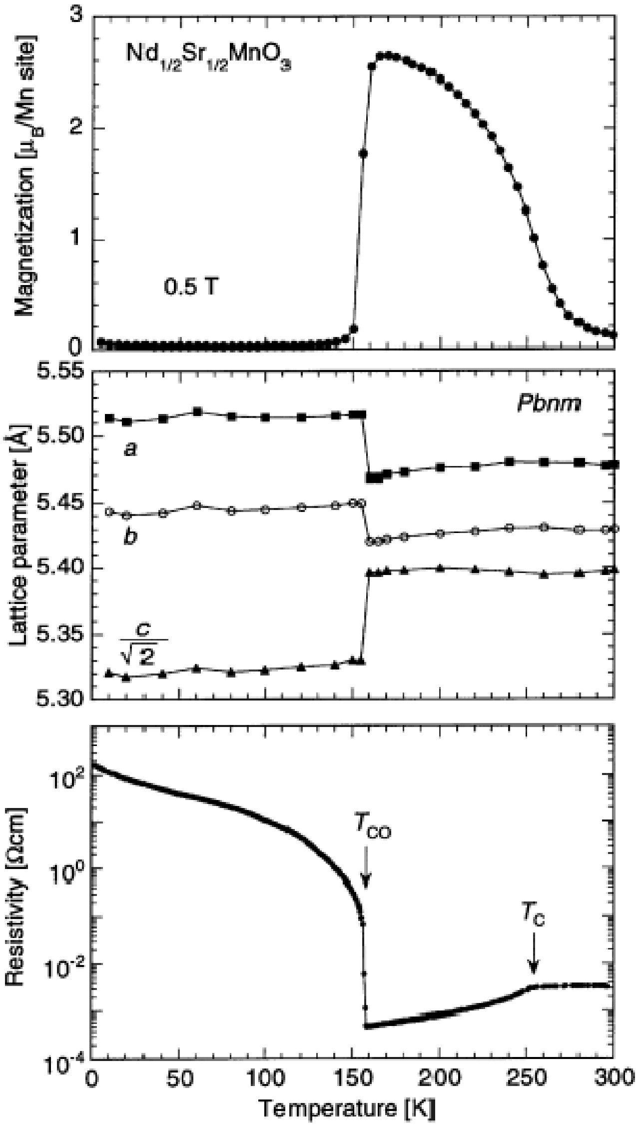

Fig.1.22. The temperature dependence of magnetization (top), resistivity (middle) and lattice parameters (bottom) observed for bulk $Nd_{0.5}Sr_{0.5}MnO_3$. In $Nd_{0.5}Sr_{0.5}MnO_3$ the critical temperature of the charge/orbital ordering transition coincides with the antiferromagnetic Neel temperature (T_{CO}=T_N≈160 K) [after Tokura et al. (1999)].

In $Nd_{0.5}Sr_{0.5}MnO_3$, the ferromagnetic and metallic state due to the double-exchange (DE) interaction is seen below T_C=255 K, and subsequently the transition to the antiferromagnetic charge/orbital- ordered state occurs at T_{CO} (= T_N) ≈ 160 K [Kuwahara et al. (1995)].

1.9.7 Structure, Phase Transition and Magnetic Behavior of Nanocrystalline $Nd_{0.5}Sr_{0.5}MnO_3$ Manganites

Recently Biswas et al. (2007) reported the effect of the reduction of particle size on the structure and magnetic properties of $Nd_{0.5}Sr_{0.5}MnO_3$ [NSMO]. The temperature dependence of zero field cooled (ZFC) and field cooled (FC) direct current (dc) susceptibility $\chi(T)$ data on two nanocrystalline NSMO samples reported by Biswas et al. (2007) is shown in Fig. 1.23. Large bifurcation has been observed between zero field cooled and field cooled $\chi(T)$ (Fig. 1.23). In addition to this, ZFC as well as FC susceptibility drops quite sharply below ~20 K. As shown in inset to Fig. 1.23, the temperature dependence of $d\chi/dT$ shows sharp minima at T_C. Evidently, for both the samples, T_C is reduced in comparison with that of the bulk $Nd_{0.5}Sr_{0.5}MnO_3$ [Kuwahara et al. (1995); Lopez et al. (2001)]. For 30 nm sample, T_C is ~230 K and that for 55 nm sample it is ~235 K. Biswas et al. (2007) proposed that the reduction in T_C is due to the weakening of DE interaction. In case of 55 nm sample, the experimentally obtained μ_{eff} agrees quite well with the theory whereas for 30 nm sample, it does not. Many authors reported that the magnetic properties of the nanoparticles can be influenced by the disorder effect [Biswas et al. (2005); Kodama et al. (1996); Coey (1971); Wang et al. (2000); Morales et al. (2004)].

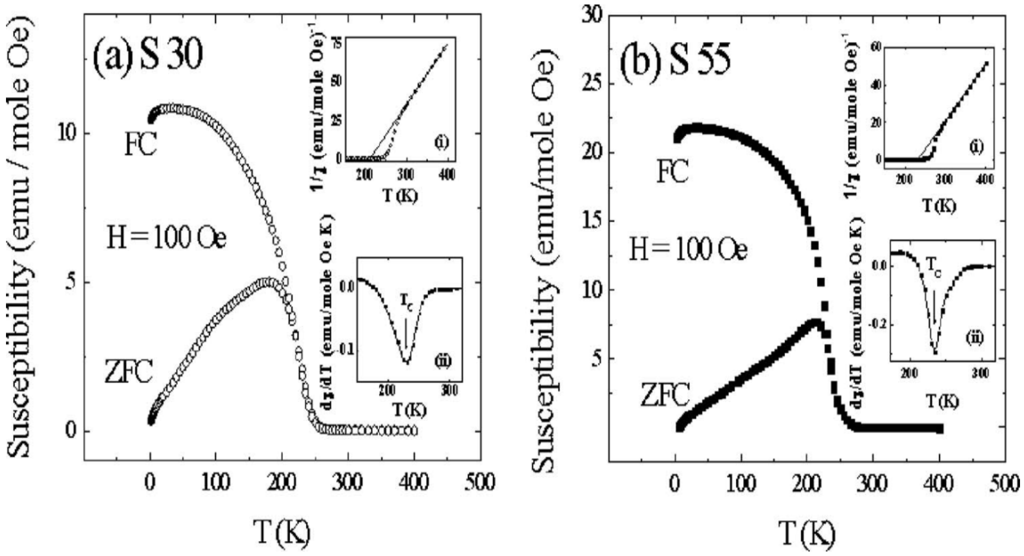

Fig. 1.23. Temperature dependence of field cooled and zero field cooled susceptibility for (a) S30 (30 nm) and (b) S55 (55 nm). The measurements have been performed in the presence of 100 Oe magnetic field. Insets: a(i) and b(i). Temperature dependence of inverse zero field cooled susceptibility in high temperature region for S30 (30 nm) and S55 (55 nm), respectively. The temperature region above 300 K has been fitted according to the Curie–Weiss function, $\chi \approx C/T-\theta_p$. a(ii) and b(ii). The minima at temperature dependence of $d\chi/dT$ indicated by arrow represent the paramagnetic to ferromagnetic transition [after Biswas et al. (2007)].

The surface layers, comprising the noncollinear arrangements of spins as well as dislocations and vacancies, are always in disordered states [Biswas et al. (2005); Kodama et al. (1996); Coey (1971); Wang et al. (2000)]. In addition to this, disorder can also be present inside the particle, which is reflected in the magnetic behavior of the systems, e.g., the broadness of magnetic transition, the deviation of $\chi(T)$ from the Curie–Weiss law in paramagnetic state, etc. [Morales et al. (2004)]. Biswas et al. (2007) reported that the surface disorder effect is large in the case of 30 nm sample, which is manifested in the reduction of the value of μ_{eff} than the theoretically predicted one. On the other hand, such an effect is considerably small for 55 nm sample because of its relatively large particle size. Biswas et al. (2007) proposed that due to the existence of the disordered surface layers, magnetic frustration may occur, which can give rise to a cluster glasslike magnetic state in the nanoparticles. The bifurcation between the FC and ZFC curve can be considered as an indication of such a glassy magnetic state [[Biswas et al. (2005); Wang et al. (2000)]. The most striking feature of the temperature dependence of susceptibility for the nanocrystalline samples is the absence of ferromagnetic to charge ordered antiferromagnetic transition.

Recently S. Kundu et. al. (2012), also investigated the crystal structure and magnetic behavior of nanocrystalline $Nd_{0.5}Sr_{0.5}MnO_3$. Fig. 1.24 depicts the variation of lattice parameters with measuring temperature for nanocrystalline and bulk $Nd_{0.5}Sr_{0.5}MnO_3$ manganites reported by Kundu et al. (2012). The estimated lattice parameters of bulk NSMO1150 are in agreement with those reported in the literature for the bulk samples [Machida et al. (2000)].

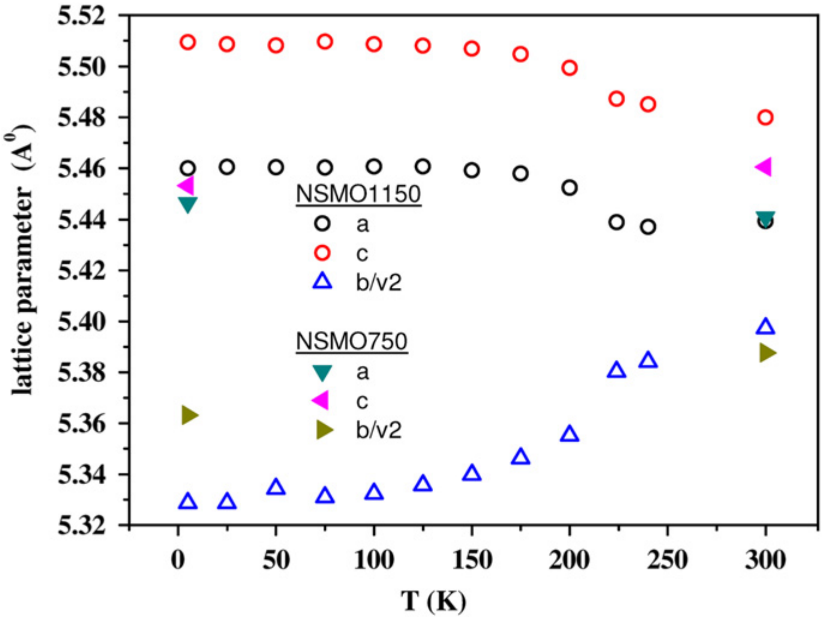

Fig. 1.24. Variation of lattice parameters of NSMO1150 (bulk) and NSMO750 (nano) samples with temperature obtained from refinement of neutron diffraction data [after Kundu et al. (2012)].

The absence of the CE-type ordering in nano samples indicates that the CE-type ordering is very sensitive to particle size and even a reduction of particle size to 800 nm suppresses it. The zero field-cooled (ZFC) and field-cooled (FC) temperature dependent magnetization data recorded at 500 Oe field during heating cycle reported by Kundu et al. (2012) is shown in Fig. 1.25. The NSMO1150 (bulk) sample clearly shows the FM–PM (para-magnetic) transition at around 250K (T_C) and the FM–AFM transition at around 150K. The transition temperatures are in agreement with those reported in literature for bulk samples [Tokura (2000)]. In contrast, the nano samples NSM0750 and NSM0850 exhibit magnetization behavior distinct from bulk NSMO1150 sample. The ZFC magnetization of nano (NSMO750 and NSMO850) samples increases with the increase of temperature, exhibits a peak, and there after falls broadly around 250K. A strong bi-furcation of the FC and ZFC magnetization curves shown in Fig. 1.25 indicates the presence of a high level of anisotropy in the nano samples. These behaviors indicate that in the low temperature regime a blocked ferromagnetic state might form as a result of nanocrystalline grain size as well as from destabilization of the AFM order into a FM state [Jirak et al. (2010); Pramanik et al. (2010)]. The plot of $d(M_{ZFC}–M_{FC})/dT$ vs. T is known to represent the distribution of blocking temperatures ($f(T_B)$) in nano samples [Knobel et al. (2008)]. The plot of $f(T_B)$ as function of temperature reported by Kundu et al. (2102) is shown in the insets of Fig. 1.26. The temperature where the peak in the $f(T_B)$ occurs is the average blocking temperature of the system. It is seen that the peak in the $f(T_B)$ for NSMO750 sample occurs around a lower temperature compared to that for NSMO850 sample.

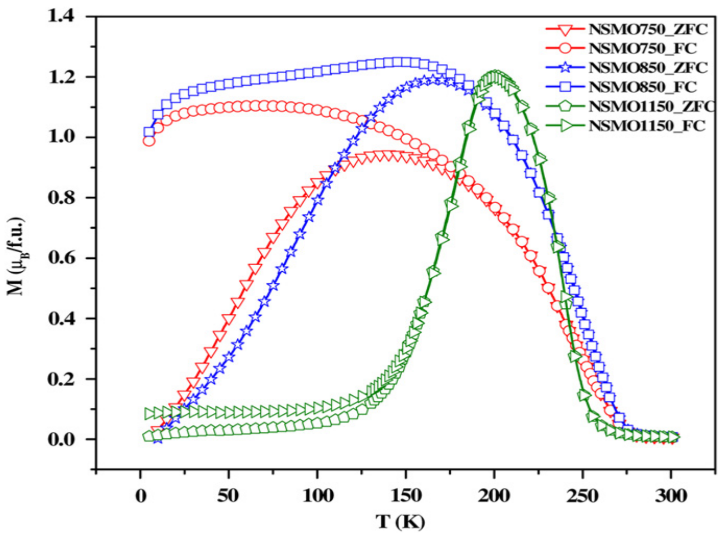

Fig. 1.25. Temperature variation of zero field cooled (ZFC) and field cooled (FC) magnetization of NSMO1150 (bulk), NSMO850 (nano) and NSMO750 (nano) samples measured at 500 Oe magnetic field [after Kundu et al. (2012)].

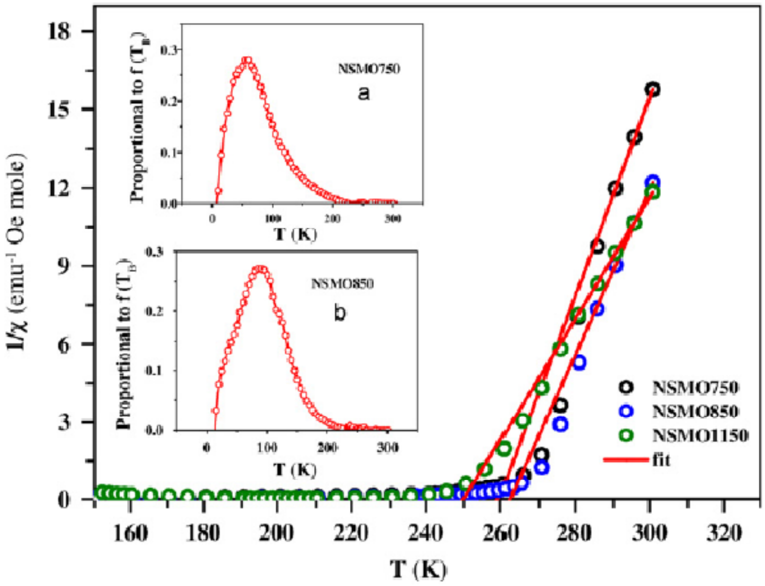

Fig. 1.26. Plot of 1/χ vs. T for bulk and nano NSMO samples. The straight line represents the fitted curve under Curie–Weiss law.The insets (a) and (b) display the distribution of blocking temperatures (T_B) of NSMO750 and NSMO850 samples, respectively [after Kundu et al. (2012)].

This is consistent with the fact that NSMO750 sample has a smaller average grain size compared to NSMO850 sample. The M–H hysteresis behaviors of the bulk and nano samples reported by Kundu et al. (2012) are shown in the Fig. 1.27. The M–H curves at 60K of NSMO750 (nano) and at 100K for NSMO850 (nano) samples demonstrate ferromagnetic behavior with large coercivity. Ferromagnetic nature of the samples and presence of spontaneous magnetization is also evident from the positive intercept in the Arrott plots shown in the inset (a) for NSMO850 sample and in the inset (b) for NSMO750 sample of Fig. 1.27. Kundu et al. (2012) reported that the calculated values of spontaneous magnetizations were 1.75 μ_B/f.u. for NSMO750 (60K) and 1.87 μ_B/f.u. for NSMO850 (100K) samples. This suggests that double exchange mechanism, primarily responsible for FM states in the manganites, begins to dominate over the super-exchange in nanometric samples. Kundu et al. (2012) also reported that, the calculated saturation magnetization of NSMO750 (nano) sample at 60K (1.90 μ_B/f.u.) is smaller than that calculated in the ferromagnetic regime of the NSMO1150 (bulk) (2.60 μ_B/f.u., at 200K) sample. The reduced values of the magnetic moment in comparison to the expected moment in nano samples, has also been reported in other similar studies [Zirak et al. (2010)]. This was attributed to the presence of a non-magnetic shell surrounding the core in nano perovskite manganites.

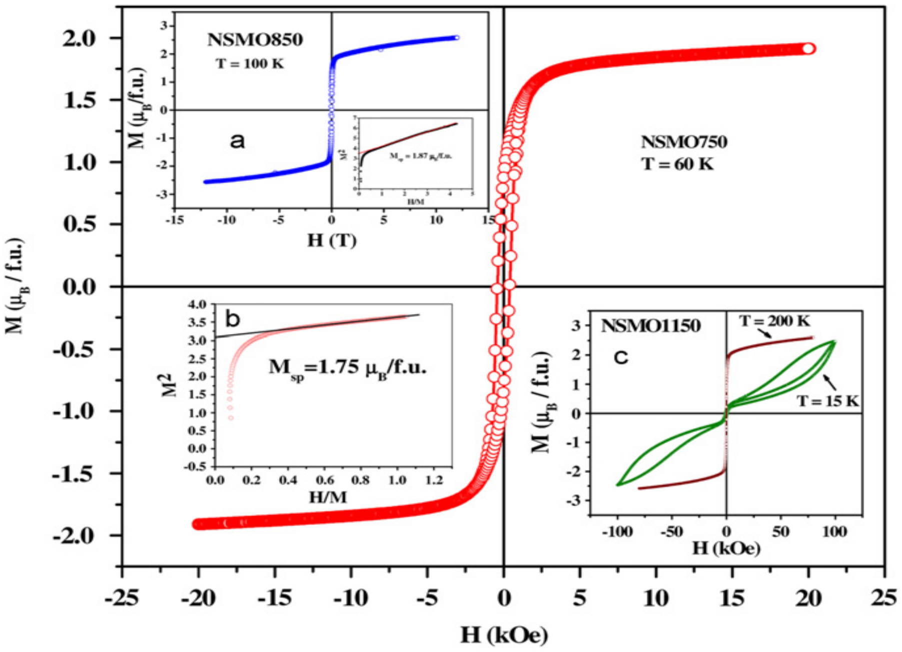

Fig. 1.27. Hysteresis behavior (M–H loop) of NSMO750 (nano) sample measured at 60K. Inset (a) shows the M–H loop at 100K for NSMO850 (nano) sample and Arrott plot utilizing the same. Inset (b) shows the Arrott plot for NSMO750 sample at 60K. Inset (c) shows the M–H loops at 15K and 200K for NSMO1150 (bulk) sample [after Kundu et al. (2012)].

1.9.8 Magnetic Behavior and Phase Transitions in $Sm_{1-x}Ca_xMnO_3$ Manganites

The magnetic phase diagram of $Sm_{1-x}Ca_xMnO_3$ reported by Martin et al. (1999) is shown in Fig. 1.28. The magnetic phase diagram of $Sm_{1-x}Ca_xMnO_3$ manganites, is characterized by low radii $<r_A>$ of cations at A site, ranging from 1.132 to 1.180 Å, in the entire composition range. The tolerance factor of this perovskite is always lower than 1 and increases with x (calcium content). Therefore, the SCMO exhibits highly distorted $GdFeO_3$-type structures that are favorable for the charge localization and detrimental for the DE interactions. Consequently, no ferromagnetic metallic state is detected in all the hole doped region of SCMO samples (see Fig. 1.28). A ferromagnetic insulating (FMI) region is observed in SCMO for $x<0.35$. The value of magnetization of SCMO at 4 K increases with x, reaches a maximum value of $2.5\mu_B$ at $x = 0.20$, and decreases again abruptly (see dashed line in Fig. 1.28). The SCMO is reported to exhibit a *Pnma* structure in the paramagnetic state at room temperature but the low temperature phases are quite different for different compositions [Martin et al. (1999)]. At 10 K, $Sm_{0.15}Ca_{0.85}MnO_3$ exhibits a $P2_1/m$ space group associated with a C-type AFM structure and $Sm_{0.10}Ca_{0.90}MnO_3$ is characterized by a *Pnma* space group with a G-type AFM structure with a FM component [Zirak et al. (1985)].

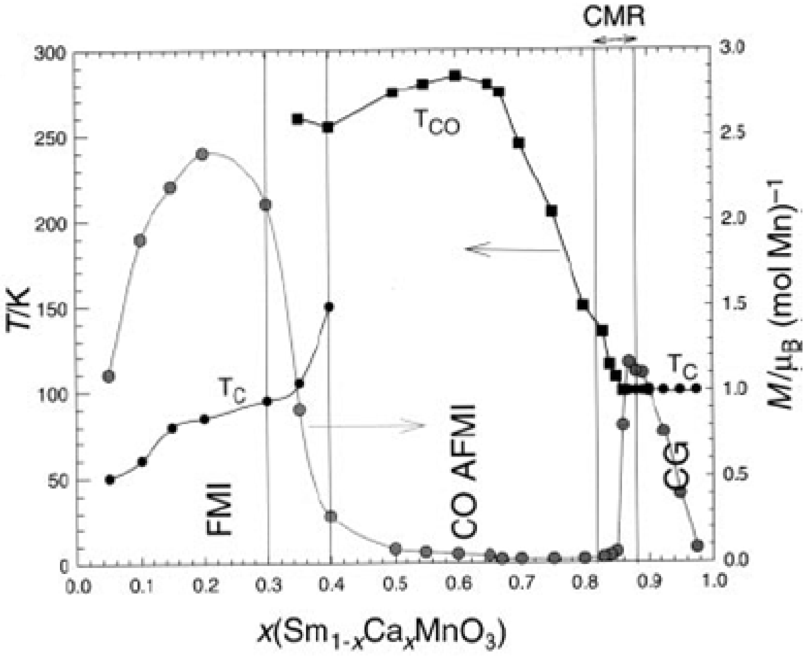

Fig. 1.28. Magnetic phase diagram for the $Sm_{1-x}Ca_xMnO_3$, solid circle, solid square, and solid triangles represent T_C, T_{CO}, and T_N, respectively for different compositions. The two hatched zones represent the intermediate regions, and the CMR domain is shown by arrows in the upper part [after Martin et al. (1999)].

1.9.9 Lattice parameter, Unit Cell Volume, Magnetization and Resistivity variation in $Sm_{0.5}Ca_{0.5}MnO_3$ Manganites

Fig. 1.29 shows the temperature dependence of resistivity, magnetization and lattice parameters for $Sm_{0.5}Ca_{0.5}MnO_3$ sample reported by Tokura et al. (1999). The charge/orbital ordering transitions manifest themselves as decrease in magnetization and increase in resistivity, at $T_{CO} \approx 270$ K in bulk $Sm_{0.5}Ca_{0.5}MnO_3$. The lattice parameters also show discontinuous change at T_{CO}; as elongation in the orthorhombic a- and b-axes and contraction in the c-axis, which suggests that ordering of e_g-orbital, occurs simultaneously. Such a change in lattice parameters upon the charge/orbital ordering transition is also shown in Fig. 1.13 for bulk polycrystalline $La_{0.5}Ca_{0.5}MnO_3$ (T_{CO} (= T_N) ≈ 160 K) [Radaelli et al. (1995); Radaelli et al. (1997)]. In bulk samples of $Sm_{0.5}Ca_{0.5}MnO_3$, similar changes in resistivity and magnetization are seen at $T_{CO} \approx 270$ K [Tomioka et al. (1997)], where the charge/orbital ordering takes place. However, as seen in the magnetization data the antiferromagnetic spin-ordering occurs at a lower temperature, $T_N \approx 170$ K, and no ferromagnetic state is present at zero fields. In the reduced-bandwidth systems, such as $RE_{0.5}Ca_{0.5}MnO_3$ (RE = Pr, Nd, Sm, etc.), in which no ferromagnetic or metallic state is realized, a split between T_{CO} and T_N is generally observed. A similar feature is also observed for the related material with the layered-perovskite structure, $La_{1-x}Sr_{1+x}MnO_4$ ($x = 1/2$), where $T_{CO} \approx 217$ K and $T_N \approx 110$ K [Sternlieb et al. (1996)].

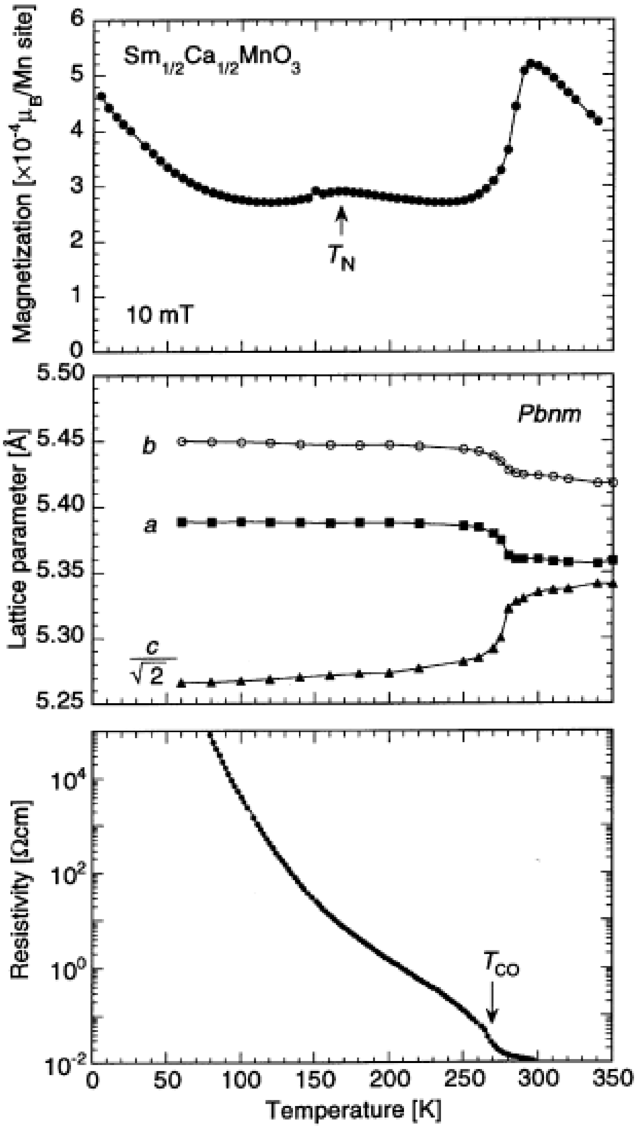

Fig. 1.29. The temperature dependencies of magnetization (top), resistivity (middle) and lattice parameters (bottom) observed for bulk $Sm_{0.5}Ca_{0.5}MnO_3$ sample, ($T_{CO} \approx 270$ K and $T_N \approx 170$ K) [after Tokura et al. (1999)].

1.9.10 Magnetic Behaviour of Nanocrystalline half doped $Sm_{0.5}Ca_{0.5}MnO_3$ Manganites

Fig. 1.30 shows the zero-field-cooled (ZFC) and field-cooled (FC) magnetizations between 4 and 300 K under cooling at measuring field of 1 kOe for the nano (~70 nm) SCMO sample reported by Zhou et al. (2008). As shown in the inset of Fig. 1.30(a), the CO transition peak is seen to be decreased in the intensity in comparison to that of the bulk [Tokura et al. (2006)], which indicates that the CO phase is weakened in the nanosized SCMO. Zhou et al. (2008) did not observed visible AFM transition in the magnetization curve for the nanosized samples. Moreover, the magnetization of the nanoparticles is reported to be significantly enhanced below about 100 K, pointing out the FM tendency at low temperature. Appearance of ferromagnetism at low temperatures in nano sample is further confirmed by the hysteresis loop in the field dependent magnetization shown in Fig. 1.30 (b). The magnetic behaviors of nano SCMO samples is similar to other results reported recently in nanosized CO manganites [Rao et al. (2005); Rao et al. (2006); Zhang et al. (2007); Sarkar et al. (2007)]. In addition, similar to LCMO [Shankar et al. (2015)] and NSMO [Biswas et al. (2007)] the ZFC magnetization bifurcates from the FC below ~75 K and shows a peak at ~45 K, indicating glassy behavior at low temperatures [Zhang et al. (2007)]. Zhou et al. (2008) reported a shift to positive magnetization axis for the FC loop also, which suggests the presence of a unidirectional exchange anisotropy interaction, which drives the FM domains back to the original orientation when the magnetic field is removed [Nogues et al. (2005)].

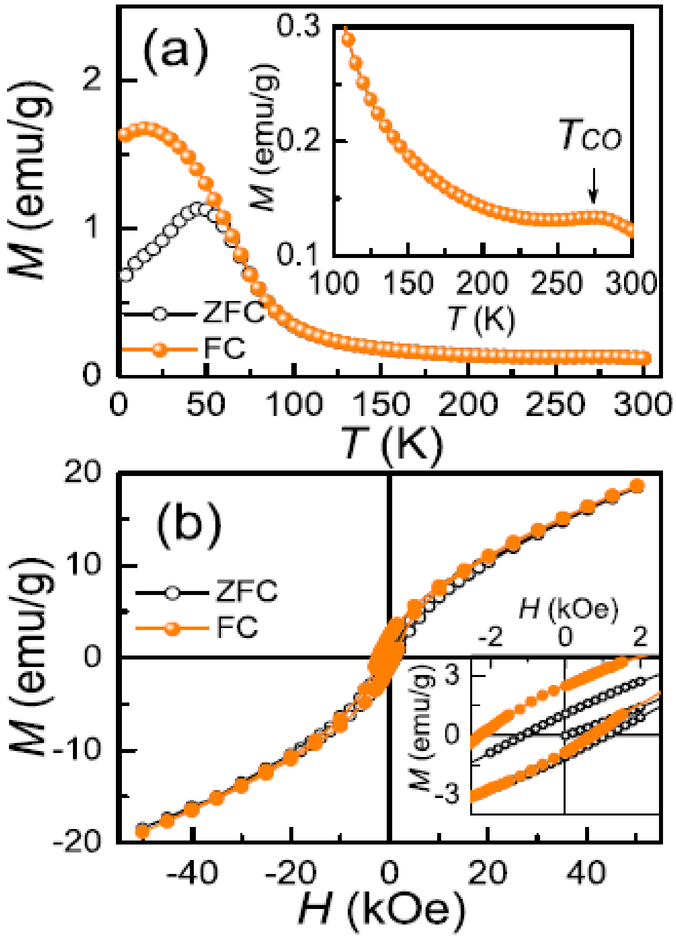

Fig. 1.31. (a) ZFC and FC magnetizations measured at H =1 kOe for the 70 nm SCMO nanoparticles. The inset to (a) shows the enlarged view of the high temperature region. (b) Hysteresis loops of magnetization at 4 K after ZFC and FC under 10 kOe for the 70 nm SCMO nanoparticles. The inset to (b) shows the enlarged view of low field region [after Zhou et al. (2008)].

Fig. 1.31 shows the FC hysteresis loops for the nanosized SCMO with the particle sizes ranging from about 1000 to 40 nm reported by Zhou et al. (2008). It is found that the sample with a smaller particle size has a larger magnetization, which suggests that the FM ordering is enhanced as the particle size is reduced. Zhou et al. (2008) proposed this behavior to be due to core shell structure similar to that reported in other nanosized CO manganites [Rao et al. (2005); Rao et al. (2006); Sarkar et al. (2007)]. Zhou et al. (2008) reported exchange bias phenomenon also in nano SCMO samples as shown in the inset of Fig. 1.31.

Recently, Giri et al. (2014) also investigated the magnetic and phase transition behavior of nanocrystalline half doped SCMO samples. The temperature dependent zero field cooled (ZFC) dc magnetization (M) of the SCMO samples reported by Giri et al. (2014) is shown in Fig. 1.32.

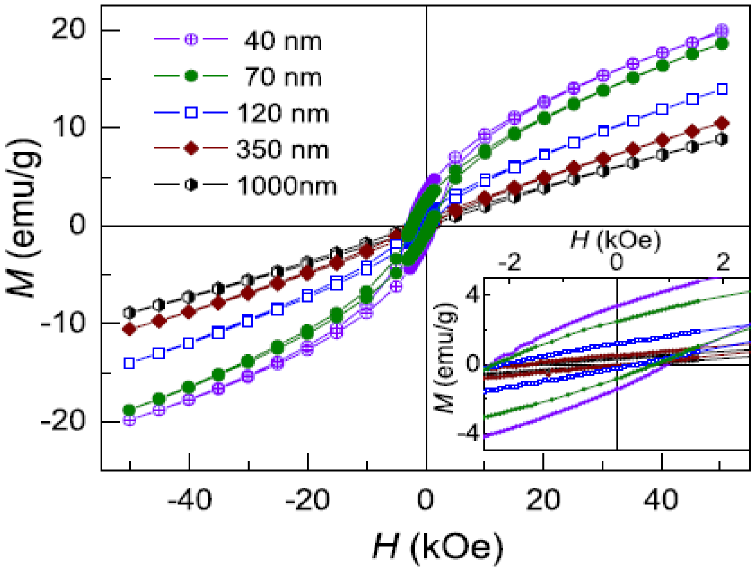

Fig. 1.31. M-H hysteresis loops at 4 K after FC under 10 kOe for the nanosized SCMO with different particle sizes. The inset shows the enlarged view of low field region [after Zhou et al. (2008)].

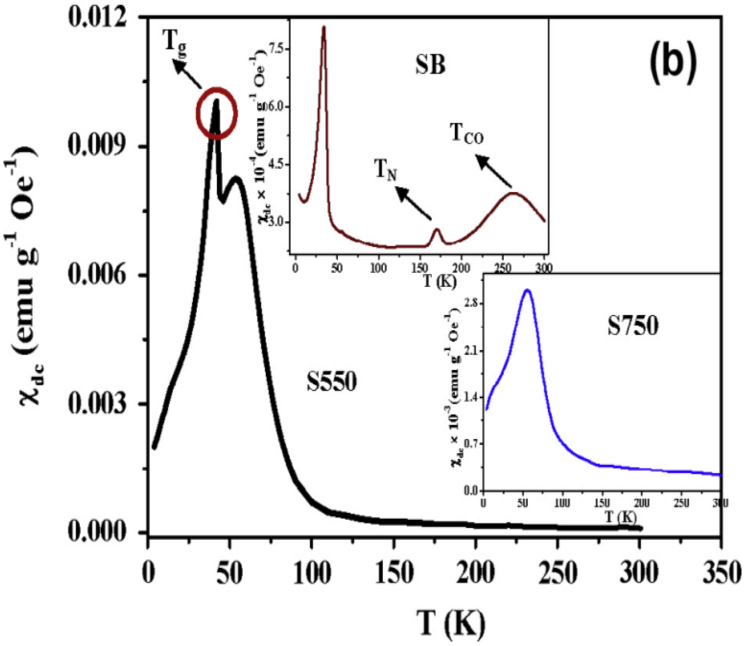

Fig. 1.32. Zero Field Cooling (ZFC) dc magnetic susceptibility plot of nano (S550), nano (S750) (lower inset) and bulk (SB) (upper inset) $Sm_{0.5}Ca_{0.5}MnO_3$ samples [after Giri et al. (2014)].

For the bulk (SB) sample, the value of M increases with decreasing T below 300 K showing a maximum at ~270 K that corresponds to the development of an AFM charge ordered state (upper inset of Fig. 1.32(b)) [Tokura et al. (1999); Lopez et al. (2004)]. For the nano (S750) sample (lower inset of Fig. 1.32(b)), in addition to the low temperature cluster glass (CG) state, a peak (~54 K) of FM to PM like transition at higher temperature due to the appearance of FM ordering is also seen. In case of the nano (S550) sample (Fig. 1.32(b)), magnetization rises monotonically as the temperature is lowered with a small shoulder at the vicinity of T = 41 K. For nano (S550), a glassy transition is observed besides the FM to PM transition. Giri et al. (2014) also reported that for SCMO nanoparticles, the nature of magnetization is different from that observed in the bulk samples, and there is a large enhancement of magnetic moment at low temperatures due to the enhanced surface effect. Giri et al. (2014) reported Griffiths phase like behavior also in nano SCMO samples. The downturn nature of χ^{-1} as a function of temperature is considered as characteristic of the Griffiths singularity in magnetic systems [Deisenhofer et al. (2005); Salamon et al. (2003)]. The temperature dependences of dc χ^{-1} reported by Giri et al. (2014) for the bulk (SB) and nano S750 and S550 samples, are shown in Fig. 1.33(a)–(c), respectively. Griffiths phase like behavior is clearly seen below a critical temperature where M shows downturn. The onset of this downturn is denoted as T_G below which the FM clusters emerge in the paramagnetic matrix. Such a behavior is also evident in χ^{-1} ac (T) plot of the nano S550 and nano S750 samples. The values of T_G for the S550 and S750 samples are found to be ~140 K and 110 K, respectively [Zhou et al. (2008)].

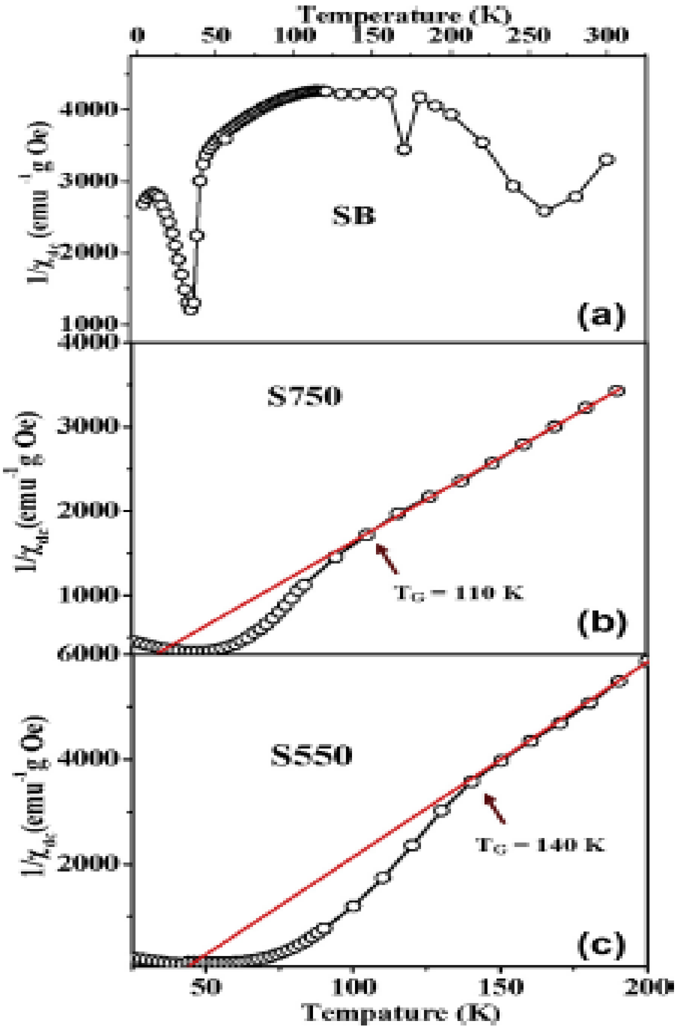

Fig. 1.33. The plot of χ^{-1} (dc) measured at H = 50 Oe as a function of temperature for (a) bulk (SB), (b) nano (S750) and (c) nano (S550) $Sm_{0.5}Ca_{0.5}MnO_3$ samples [after Giri et al. (2014)].

For the bulk (SB) sample, there is no downturn behavior but an upward deviation in χ^{-1} (T), mainly arising due to the development of CO/AFM state is seen. In high temperature regime, χ^{-1} varies linearly with T indicating the CW behavior. However, with decreasing temperature, a sharp downturn is observed in χ^{-1} (T) for the nano samples much above T_C indicating a non-analytical behavior of magnetization arising from the Griffiths singularity.

1.10 Objectives of the Present Thesis Work

Based on the detailed literature survey on bulk and nanocrystalline $R_{0.5}A_{0.5}MnO_3$ (R = La, Nd, Pr, Sm and A = Ca, Sr) manganites, we decided to investigate following important aspects for the present Ph.D. thesis:

1. To synthesize stoichiometric phase pure nanocrystalline $R_{0.5}A_{0.5}MnO_3$ (R = La, Nd, Pr, Sm and A = Ca, Sr) perovskites of different crystallite sizes and investigate the structure property correlations.
2. To understand the origin of suppression of charge ordering transition in nanocrystalline $R_{0.5}A_{0.5}MnO_3$ (R = La, Nd, Pr, Sm and A = Ca, Sr) manganites.
3. To investigate the room temperature and low temperature crystal structure of nanocrystalline $R_{0.5}A_{0.5}MnO_3$ (R = La, Nd, Pr, Sm and A = Ca, Sr) manganites as a function of crystallite size.
4. To investigate the magnetic phase transition behaviour of nanocrystalline $R_{0.5}A_{0.5}MnO_3$ (R = La, Nd, Pr, Sm and A = Ca, Sr) manganites as a function of crystallite size.